

Entanglement entropy of two disjoint intervals in $c = 1$ theories

Vincenzo Alba¹, Luca Tagliacozzo², Pasquale Calabrese³

¹ Max Planck Institute for the Physics of Complex Systems, Nöthnitzer Str. 38, 01187 Dresden, Germany,

² School of Mathematics and Physics, The University of Queensland, Australia, ICFO, Institut de Ciències Fòtiques, 08860 Castelldefels (Barcelona) Spain

³ Dipartimento di Fisica dell'Università di Pisa and INFN, Pisa, Italy.

Abstract.

We study the scaling of the Rényi entanglement entropy of two disjoint blocks of critical lattice models described by conformal field theories with central charge $c = 1$. We provide the analytic conformal field theory result for the second order Rényi entropy for a free boson compactified on an orbifold describing the scaling limit of the Ashkin-Teller (AT) model on the self-dual line. We have checked this prediction in cluster Monte Carlo simulations of the classical two dimensional AT model. We have also performed extensive numerical simulations of the anisotropic Heisenberg quantum spin-chain with tree-tensor network techniques that allowed to obtain the reduced density matrices of disjoint blocks of the spin-chain and to check the correctness of the predictions for Rényi and entanglement entropies from conformal field theory. In order to match these predictions, we have extrapolated the numerical results by properly taking into account the corrections induced by the finite length of the blocks to the leading scaling behavior.

1. Introduction

Let us imagine to divide the Hilbert space \mathcal{H} of a given quantum system into two parts \mathcal{H}_A and \mathcal{H}_B such that $\mathcal{H} = \mathcal{H}_A \otimes \mathcal{H}_B$. When the system is in a pure state $|\Psi\rangle$, the bipartite entanglement between A and its complement B, can be measured in terms of the Rényi entropies [1]

$$S_A^{(n)} = \frac{1}{1-n} \log \text{Tr} \rho_A^n, \quad (1)$$

where $\rho_A = \text{Tr}_B \rho$ is the reduced density matrix of the subsystem A, and $\rho = |\Psi\rangle\langle\Psi|$ is the density matrix of the whole system. The knowledge of $S_A^{(n)}$ as a function of n identifies univocally the full spectrum of non-zero eigenvalues of ρ_A [2], and provides complementary information about the entanglement to the one obtained from the von Neumann entanglement entropy $S_A^{(1)}$. Furthermore, the scaling of $S_A^{(n)}$ with the size of A in the ground-state of a one-dimensional system is more suited than $S_A^{(1)}$ to understand if a faithful representation of the state in term of a matrix product state can be or cannot be obtained with polynomial resources in the length of the chain [3, 4].

For a one-dimensional critical system whose scaling limit is described by a conformal field theory (CFT), in the case when A is an interval of length ℓ embedded in an infinite system, the asymptotic large ℓ behavior of the quantities determining the Rényi entropies is [5, 6, 7, 8]

$$\text{Tr} \rho_A^n \simeq c_n \left(\frac{\ell}{a} \right)^{c(n-1/n)/6}, \quad \Rightarrow S_A^{(n)} \simeq \frac{c}{6} \left(1 + \frac{1}{n} \right) \log \frac{\ell}{a} + c'_n, \quad (2)$$

where c is the central charge of the underlying CFT and a the inverse of an ultraviolet cutoff (e.g. the lattice spacing). The prefactors c_n (and so the additive constants c'_n) are non universal constants (that however satisfy universal relations [9]).

The central charge is an ubiquitous and fundamental feature of a conformal field theory [10], but it does not always identify the universality class of the theory. A relevant class of relativistic massless quantum field theories are the $c = 1$ models, which describe many physical systems of experimental and theoretical interest. The one-dimensional Bose gas with repulsive interaction, the (anisotropic) Heisenberg spin chains, the Ashkin-Teller model and many others are all described (in their gapless phases) by $c = 1$ theories. These are all free-bosonic field theories where the boson field satisfies different periodicity constraints, i.e. it is compactified on a specific target space. The two most notable examples are the compactification on a circle (corresponding to the Luttinger liquid field theory) and on a Z_2 orbifold (corresponding to the Ashkin-Teller model [11, 12, 13]). The critical exponents depend in a continuous way on the compactification radius of the bosonic field. A survey of the CFTs compactified on a circle or on a Z_2 orbifold is given in Fig. 1, in a standard representation [12, 13]. The horizontal axis is the compactification radius on the circle r_{circle} , while the vertical axis represents the value of the Z_2 orbifold compactification radius r_{orb} . The two axes cross in a single point, meaning that the theories at $r_{\text{circle}} = \sqrt{2}$ and at $r_{\text{orb}} = 1/\sqrt{2}$ are the same. (The graph is not a cartesian plot, i.e. it has no meaning to have one r_{circle} and one r_{orb} at the same time.) For some values of r_{circle} and r_{orb} , we report statistical mechanical models and/or field theories to which they correspond. In the following we will consider the Ashkin-Teller model that on the self-dual line is described by $r_{\text{orb}} \in [\sqrt{2/3}, \sqrt{2}]$ and the XXZ spin

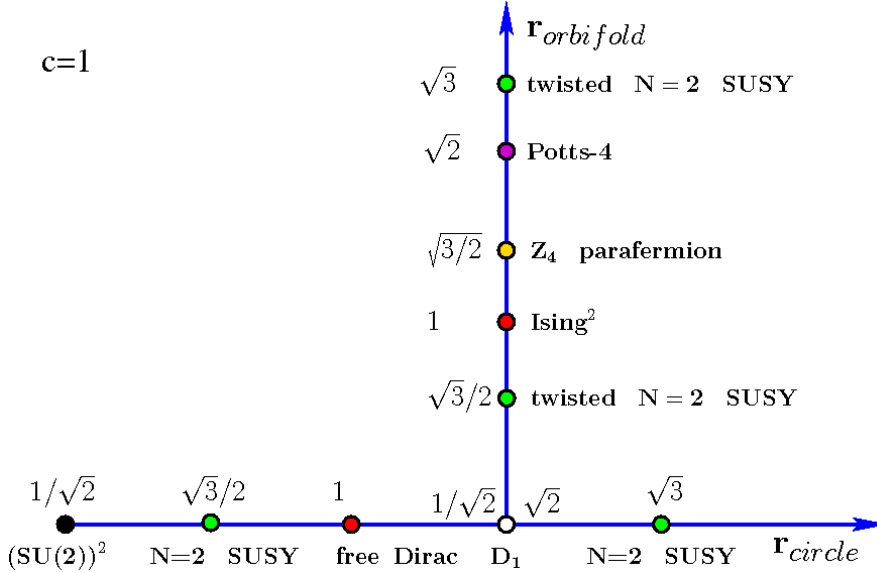


Figure 1. Survey of $c = 1$ theories corresponding to a free boson compactified on a circle (horizontal axis) and on an orbifold (vertical axis) as reported e.g. in Refs. [12]. For some values of r_{circle} and r_{orb} , the corresponding statistical mechanical models are reported. The XXZ spin chain in zero magnetic field lies on the horizontal axis in the interval $r_{\text{circle}} \in [0, 1/\sqrt{2}]$. The self-dual line of the Ashkin-Teller model lies on the vertical axis in the interval $r_{\text{orb}} \in [\sqrt{2/3}, \sqrt{2}]$.

chain in zero magnetic field that is described by $r_{\text{circle}} \in [0, 1/\sqrt{2}]$. We mention that different compactifications have been studied [14], but they correspond to more exotic statistical mechanical models and will not be considered here.

According to Eq. (2), the central charge of the CFT can be extracted from the scaling of both the Rényi and von Neumann entropies. In the last years, this idea has overcome the previously available techniques of determining c , e.g. by measuring the finite size corrections to the ground state energy of a spin chain [15]. However, the dependence of the scaling of the entropies of a single block only on the central charge prevents to extract from them other important parameter of the model such as the compactification radius. It has been shown that instead the entanglement entropies of disjoint intervals are sensitive to the full operator content of the CFT and in particular they depend on the compactification radius and on the symmetries of the target space. Thus they encode complementary information about the underlying conformal field theory of a given critical quantum/statistical system to the knowledge of the central charge present in the scaling of the single block entropies. (Oppositely in 2D systems with conformal invariant wave-function, the entanglement entropy of a single region depends on the compactification radius [16].)

This observation boosted an intense theoretical activity aimed at determining Rényi entropies of disjoint intervals both analytically and numerically [17, 18, 19, 20, 21, 22, 23, 24, 25, 26, 27, 28, 29, 30]. A part of this paper is dedicated to consolidate some of the results already provided in other works where they either have been studied only on very small chains, with the impossibility of properly taking into account the severe finite size corrections [17] or have been tested in the specific cases of spin chains

equivalent to free fermionic models [24, 26]. An important point to recall when dealing with more than one interval is that the Rényi entropies in Eq. (1) measure only the entanglement of the disjoint intervals with the rest of the system. They do *not* measure the entanglement of one interval with respect to the other, that instead requires the definition of more complicated quantities because $A_1 \cup A_2$ is in a mixed state (see e.g. Refs. [31] for a discussion of this and examples). Furthermore, it must be mentioned that some results about the entanglement of two disjoint intervals are at the basis of a recent proposal to "measure" the entanglement entropy [32].

1.1. Summary of some CFT results for the entanglement of two disjoint intervals

We consider the case of two disjoint intervals $A = A_1 \cup A_2 = [u_1, v_1] \cup [u_2, v_2]$. By global conformal invariance, in the thermodynamic limit, $\text{Tr } \rho_A^n$ can be written as

$$\text{Tr } \rho_A^n = c_n^2 \left(\frac{|u_1 - u_2||v_1 - v_2|}{|u_1 - v_1||u_2 - v_2||u_1 - v_2||u_2 - v_1|} \right)^{\frac{c}{6}(n-1/n)} F_n(x), \quad (3)$$

where x is the four-point ratio (for real u_j and v_j , x is real)

$$x = \frac{(u_1 - v_1)(u_2 - v_2)}{(u_1 - u_2)(v_1 - v_2)}. \quad (4)$$

The function $F_n(x)$ is a universal function (after being normalized such that $F_n(0) = 1$) that encodes all the information about the operator spectrum of the CFT and in particular about the compactification radius. c_n is the same non-universal constant appearing in Eq. (2).

Furukawa, Pasquier, and Shiraishi [17] calculated $F_2(x)$ for a free boson compactified on a circle of radius r_{circle}

$$F_2(x) = \frac{\theta_3(\eta\tau)\theta_3(\tau/\eta)}{[\theta_3(\tau)]^2}, \quad (5)$$

where θ_ν are Jacobi theta functions and the (pure-imaginary) τ is given by

$$x = \left[\frac{\theta_2(\tau)}{\theta_3(\tau)} \right]^4, \quad \tau(x) = i \frac{{}_2F_1(1/2, 1/2; 1; 1-x)}{{}_2F_1(1/2, 1/2; 1; x)}. \quad (6)$$

η is a universal critical exponent related to the compactification radius $\eta = 2r_{\text{circle}}^2$.[‡] This has been extended to general integers $n \geq 2$ in Ref. [19]

$$F_n(x) = \frac{\Theta(0|\eta\Gamma)\Theta(0|\Gamma/\eta)}{[\Theta(0|\Gamma)]^2}, \quad (7)$$

where Γ is an $(n-1) \times (n-1)$ matrix with elements [19]

$$\Gamma_{rs} = \frac{2i}{n} \sum_{k=1}^{n-1} \sin\left(\pi \frac{k}{n}\right) \beta_{k/n} \cos\left[2\pi \frac{k}{n}(r-s)\right], \quad (8)$$

and

$$\beta_y = \frac{{}_2F_1(y, 1-y; 1; 1-x)}{{}_2F_1(y, 1-y; 1; x)}. \quad (9)$$

[‡] Because of the symmetry $\eta \rightarrow 1/\eta$ or $r_{\text{circle}} \rightarrow 1/2r_{\text{circle}}$ for any conformal property one could also define $\eta = 1/2r_{\text{circle}}^2$ as sometimes done in the literature. However, corrections to scaling are not symmetric in $\eta \rightarrow 1/\eta$ and this is often source of confusion. A lot of care should be used when referring to one or another notation.

η is the same as above, while Θ is the Riemann-Siegel theta function

$$\Theta(0|\Gamma) \equiv \sum_{m \in \mathbf{Z}^{\alpha-1}} \exp [i\pi m^t \cdot \Gamma \cdot m]. \quad (10)$$

The analytic continuation of Eq. (7) to real n for general values of η and x (to obtain the von Neumann entanglement entropy) is still an open problem, but results for $x \ll 1$ and $\eta \ll 1$ are analytically known [19, 30].

The function $F_n(x)$ is known exactly for arbitrary integral n also for the critical Ising field theory [30]. However, in the following we will need it only at $n = 2$ (i.e. $F_2(x)$) for which it assumes the simple form [24]

$$F_2^{\text{Is}}(x) = \frac{1}{\sqrt{2}} \left[\left(\frac{(1 + \sqrt{x})(1 + \sqrt{1-x})}{2} \right)^{1/2} + x^{1/4} + ((1-x)x)^{1/4} + (1-x)^{1/4} \right]^{1/2}. \quad (11)$$

In Ref. [30], it has been proved that in any CFT the function $F_n(x)$ admits the small x expansion

$$F_n(x) = 1 + \left(\frac{x}{4n^2} \right)^\alpha s_2(n) + \left(\frac{x}{4n^2} \right)^{2\alpha} s_4(n) + \dots, \quad (12)$$

where α is the lowest scaling dimension of the theory. The functions $s_j(n)$ are calculable from a modification of the short-distance expansion [30], and in particular it has been found [30]

$$s_2(n) = \mathcal{N} \frac{n}{2} \sum_{j=1}^{n-1} \frac{1}{[\sin(\pi \frac{j}{n})]^{2\alpha}}, \quad (13)$$

where the integer \mathcal{N} counts the number of inequivalent correlation functions giving the same contribution. This expansion has been tested against the exact results for the free compactified boson (Ising model) with $\alpha = \min[\eta, 1/\eta]$ ($\alpha = 1/4$) and $\mathcal{N} = 2$ ($\mathcal{N} = 1$).

All the results we reported so far are valid for an infinite system. Numerical simulations are instead performed for finite, but large, system sizes. According to CFT [8], we obtain the correct result for a chain of finite length L by replacing all distances u_{ij} with the *chord distance* $L/\pi \sin(\pi u_{ij}/L)$ (but different finite size forms exist for excited states [33]). In particular the single interval entanglement is [6]

$$\text{Tr} \rho_A^n \simeq c_n \left[\frac{L}{\pi a} \sin \left(\frac{\pi \ell}{L} \right) \right]^{-c(n-1/n)/6}, \quad (14)$$

and for two intervals, in the case the two subsystems A_1 and A_2 have the same length ℓ and are placed at distance r , the four-point ratio x is

$$x = \left(\frac{\sin \pi \ell / L}{\sin \pi (\ell + r) / L} \right)^2. \quad (15)$$

1.2. Organization of the paper

In this paper we provide accurate numerical tests for the functions $F_n(x)$ in truly interacting lattice models described by a CFT with $c = 1$. In Sec. 2 we derive the CFT prediction for the function $F_2(x)$ of a free boson compactified on an orbifold describing, among the other things, the self-dual line of the AT model when $r_{\text{orb}} \in [\sqrt{2/3}, \sqrt{2}]$. In order to check this result, we needed to develop a classical Monte Carlo algorithm in Sec. 3 based on the ideas introduced in Ref. [18]. This algorithm is used in Sec. 4

to determine $F_2(x)$ for several points on the self-dual line. We also consider the XXZ spin-chain in zero magnetic field to test the correctness of Eq. (7). In order to extend the results of Ref. [17] to longer chains, we have used a tree tensor network algorithm that has allowed us to study chains of length up to $L = 128$ with periodic boundary conditions. In this way, we have been able to perform a detailed finite size analysis that was difficult solely with the data from exact diagonalization reported in Ref. [17]. The analysis also shows that only through the knowledge of the unusual corrections to the leading scaling behavior [34, 35, 36, 37, 38, 26] we are able to perform a quantitative test of Eq. (7). The tree tensor network algorithm is described in Sec. 5, while the numerical results are presented in Sec. 6. The various sections are independent one from each other, so that readers interested only in some results should have an easy access to them without reading the whole paper.

2. $n = 2$ R enyi entanglement entropy for two intervals in the Ashkin-Teller model

In a quantum field theory $\text{Tr } \rho_A^n$ for integer n is proportional to the partition function on an n -sheeted Riemann surface with branch cuts along the subsystem A , i.e. $\text{Tr } \rho_A^n = Z_n(A)/Z_1^n$ where $Z_n(A)$ is the partition function of the field theory on a conifold where n copies of the manifold $\mathcal{R} = \text{system} \times R^1$ are coupled along branch cuts along each connected piece of A at a time-slice $t = 0$ [8, 39]. Specializing to CFT, for a single interval on the infinite line, this equivalence leads to Eq. (2) [6], whose analytic continuation to non-integer n is straightforward. When the subsystem A consists of N disjoint intervals (always in an infinite system), the n -sheeted Riemann surface $\mathcal{R}_{n,N}$ has genus $(n - 1)(N - 1)$ and cannot be mapped to the complex plane so that the CFT calculations become more complicated.

However, for two intervals ($N = 2$), when for a given theory the partition function on a generic Riemann surface of genus g with arbitrary *period matrix* is known, $\text{Tr } \rho_A^n$ can be easily deduced exploiting the results of Refs. [19, 30]. In fact, a by-product of the calculation for the free boson [19] is that the $(n - 1) \times (n - 1)$ period matrix is always given by Eq. (8). Although derived for a free boson, the period matrix is a pure geometrical object and it is only related to the structure of the world-sheet $\mathcal{R}_{n,2}$ and so it is the same for any theory. This property has been used in Ref. [30] to obtain $F_n(x)$ for the Ising universality class for any n , in agreement with previously known numerical results [26]. When also $n = 2$, the surface $\mathcal{R}_{2,2}$ is topologically equivalent to a torus for which the partition function is known for most of the CFT. The torus modular parameter τ is related to the four-point ratio by Eq. (6). Thus, the function $F_2(x)$ is proportional to the torus partition function where τ is given by Eq. (6) and with the proportionality constant fixed by requiring $F_2(0) = 1$. This way of calculating $S_A^{(2)}$ is much easier than the general one for $S_A^{(n)}$ [40, 19] and indeed it has been used to obtain the first results both for the free compactified boson [17] and for the Ising model [24].

For a conformal free bosonic theory with action

$$S = \frac{1}{2\pi} \int dzd\bar{z} \partial\phi\bar{\partial}\phi, \quad (16)$$

the torus partition functions are known exactly both for circle and orbifold compactification [41, 42, 12].

We now recall some well-known facts in order to fix the notations and derive the function $F_2(x)$ for the Ashkin-Teller model. The bosonic field ϕ is said to be compactified on a circle of radius r_{circle} when $\phi = \phi + 2\pi r_{\text{circle}}$. The torus partition function (and the one on the n -sheeted Riemann surface) should be derived with this constraint. It is a standard CFT exercise to calculate the resulting torus partition function [41, 12]

$$Z_{\text{circle}}(\eta) = \frac{\theta_3(\eta\tau)\theta_3(\tau/\eta)}{|\eta_D(\tau)|^2}, \quad (17)$$

where $\eta_D(\tau)$ is the Dedekind eta function and $\eta = 2r_{\text{circle}}^2$. Using Eq. (6) and some properties of the elliptic functions, Eq. (5) for $F_2(x)$ follows [17]. When specialized at $\eta = 1/2$ (or $\eta = 2$), $F_2(x)$ has the simple form

$$F_2^{\text{XX}}(x) = \sqrt{(1+x^{1/2})(1+(1-x)^{1/2})}/2, \quad (18)$$

that describes the XX spin-chain (that is equivalent to free fermions via the non-local Jordan-Wigner transformation).

The concept of orbifold emerges naturally in the context of theories whose Hilbert space admits some discrete symmetries. Let us assume that G is a discrete symmetry. For the free bosonic theory, the simplest example is the one we are interested in, i.e. the Z_2 symmetry. It acts on the point of the circle S^1 in the following way

$$g : \phi \rightarrow -\phi. \quad (19)$$

For the partition function of a theory on the torus, we introduce the notation [12]

$$\pm \begin{array}{c} \square \\ \pm \end{array} \quad (20)$$

where the \pm denotes the boundary conditions on the two directions on the torus. The full partition function, given a finite discrete group G , is

$$Z_{\mathcal{T}/G} = \frac{1}{|G|} \sum_{g, h \in G} g \begin{array}{c} \square \\ h \end{array} \quad (21)$$

where $|G|$ denotes the number of elements in the group. The generalization to higher genus Riemann surfaces is straightforward (but it is not so easy to obtain results, see e.g. [13, 43]).

Now we specialize Eq. (21) to the case of the Z_2 symmetry. Since the action (16) is invariant under $g : \phi \rightarrow -\phi$, we have the torus partition function for the free boson on the orbifold [41, 42, 12]

$$Z_{\text{orb}} = \frac{1}{2} \left(\begin{array}{c} + \square \\ + \end{array} + \begin{array}{c} - \square \\ + \end{array} + \begin{array}{c} + \square \\ - \end{array} + \begin{array}{c} - \square \\ - \end{array} \right). \quad (22)$$

Standard CFT calculations lead to the result [12]

$$Z_{\text{orb}}(\eta) = \frac{1}{2} \left(Z_{\text{circle}}(\eta) + \frac{|\theta_3\theta_4|}{\eta_D\bar{\eta}_D} + \frac{|\theta_2\theta_3|}{\eta_D\bar{\eta}_D} + \frac{|\theta_2\theta_4|}{\eta_D\bar{\eta}_D} \right), \quad (23)$$

where all the τ arguments in θ_ν and η_D are understood. At the special point $\eta = 1/2$ (or $\eta = 2$) we get

$$Z_{\text{orb}}(\eta = 1/2) = \frac{1}{2} \left(\frac{|\theta_3|^2 + |\theta_4|^2 + |\theta_2|^2}{2|\eta_D|^2} + \frac{|\theta_3\theta_4|}{\eta_D\bar{\eta}_D} + \frac{|\theta_2\theta_3|}{\eta_D\bar{\eta}_D} + \frac{|\theta_2\theta_4|}{\eta_D\bar{\eta}_D} \right) = Z_{\text{Ising}}^2. \quad (24)$$

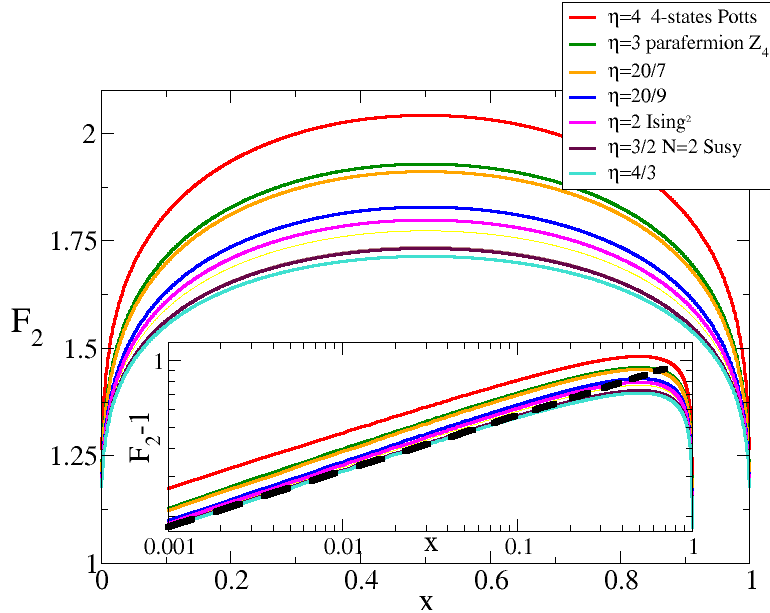


Figure 2. $F_2(x)$ for the Ashkin-Teller model on the self-dual line for some values of η . Inset: $F_2(x) - 1$ in log-log scale to highlight the small x behavior. The black-dashed line is $\sim x^{1/4}$.

Thus, from the orbifold partition function, using the last identity and normalizing such that $F_2^{AT}(0) = 1$, we can write the function $F_2^{AT}(x)$ as

$$F_2^{AT}(x) = \frac{1}{2} \left(F_2(x) - F_2^{XX}(x) \right) + (F_2^{Is}(x))^2, \quad (25)$$

where $F_2(x)$ is given in Eq. (5), $F_2^{XX}(x)$ is the same at $\eta = 1/2$ (cf. Eq. (18)) and $F_2^{Is}(x)$ is the result for Ising (cf. Eq. (11)). As a consequence of the $\eta \leftrightarrow 1/\eta$ symmetry of $F_2(x)$, also $F_2^{AT}(x)$ displays the same invariance. For small x , recalling that $F_2(x) - 1 \sim x^{\min[\eta, \eta^{-1}]}$, $F_2^{XX} - 1 \sim x^{1/2}$ and $F_2^{Is} - 1 \sim x^{1/4}$, we have

$$F_2^{AT}(x) - 1 \sim \begin{cases} x^{1/4} & \text{for } \eta \geq 1/4, \\ x^{\min[\eta, \eta^{-1}]} & \text{for } \eta \leq 1/4. \end{cases} \quad (26)$$

The critical Ashkin-Teller model lies in the interval $\sqrt{2/3} < r_{\text{orb}} < \sqrt{2}$ and so $4/3 < \eta = 2r_{\text{orb}}^2 < 4$. Thus we have $F_2^{AT}(x) - 1 \sim x^{1/4}$ along the whole self-dual line. $F_2^{AT}(x)$ for various values of η in the allowed range is reported in Fig. 2, where the behavior for small x is highlighted in the inset to show the constant $1/4$ exponent.

3. The classical Ashkin-Teller model and the Monte Carlo simulation

The two dimensional Ashkin-Teller (AT) model on a square lattice is defined by the Hamiltonian

$$H = J \sum_{\langle ij \rangle} \sigma_i \sigma_j + J' \sum_{\langle ij \rangle} \tau_i \tau_j + K \sum_{\langle ij \rangle} \sigma_i \sigma_j \tau_i \tau_j, \quad (27)$$

where σ_i and τ_i are classical Ising variables (i.e. can assume only the values ± 1). Also the product $\sigma\tau$ can be considered as an Ising variable. The model has a rich phase diagram whose features are reported in full details in Baxter's book [45]. We review in the following only the main features of this phase diagram. Under any permutation of the variables $\sigma, \tau, \sigma\tau$ the AT model is mapped onto itself. At the level of the coupling constants, this implies that the model is invariant under any permutation of J, J', K . For $K = 0$, the AT model corresponds to two decoupled Ising models in σ and τ variables. For $K \rightarrow \infty$ it reduces to a single Ising model with coupling constant $J + J'$. For $J = J' = K$ it corresponds to the four-state Potts model. It is useful to restrict to the symmetric Ashkin-Teller model where $J = J'$

$$H = J \sum_{\langle ij \rangle} (\sigma_i \sigma_j + \tau_i \tau_j) + K \sum_{\langle ij \rangle} \sigma_i \sigma_j \tau_i \tau_j. \quad (28)$$

The full phase diagram is reported in Fig. 3 (in units of the inverse temperature $\beta = 1$). The model corresponds to two decoupled critical Ising models at $K = 0$ and $2J = \log(1 + \sqrt{2})$. For $J = 0$ it is equivalent to a critical Ising model in the variable $\sigma\tau$ with critical points at $2K_{\pm} = \pm \log(1 + \sqrt{2})$. For $K \rightarrow \infty$ there are two critical Ising points at $2J = \pm \log(1 + \sqrt{2})$. On the diagonal $J = K$ the system corresponds to a 4-state Potts model which is critical at $K = (\log 3)/4$. The different kinds of orders appearing in the phase diagram are explained in the caption of Fig. 3. All the continuous lines in Fig. 3 are *critical lines*. The blue lines C-Is are in the Ising universality class. The line starting from AFIs belongs to the antiferromagnetic Ising universality class. On the red line ABC the system is critical and the critical exponents vary continuously [46, 45].

The AT model on a planar graph can be mapped to another AT model on the dual graph. When specialized to the square lattice, the phase diagram is equivalent to its dual on the self-dual line:

$$e^{-2K} = \sinh(2J). \quad (29)$$

On this line, the symmetric AT model maps onto an homogeneous six-vertex model which is exactly solvable [45]. It follows that on the self-dual line the model is critical for $K \leq (\log 3)/4$ and its critical behavior is described by a CFT with $c = 1$. Along the self-dual line the critical exponents vary continuously and are exactly known. For later convenience it is useful to parametrize the self dual line by a new parameter Δ

$$e^{4J} = \frac{\sqrt{2 - 2\Delta} + 1}{\sqrt{2 - 2\Delta} - 1}, \quad e^{4K} = 1 - 2\Delta, \quad (30)$$

with $-1 < \Delta < 1/2$. In terms of Δ , the orbifold compactification radius is [42]

$$\eta = 2r_{\text{orb}}^2 = \frac{4 \arccos(-\Delta)}{\pi} = \frac{2}{K_L}, \quad (31)$$

where K_L is the equivalent of the Luttinger liquid parameter for the AT model.

3.1. Cluster representation and Monte Carlo simulation

A Swendsen-Wang type cluster algorithm for the AT model has been proposed in Ref. [47] and then re-derived in a simpler way by Salas and Sokal [48]. Here we partly follow the derivation of Salas and Sokal and we restrict to the symmetric AT Hamiltonian (28) and assume $J \geq |K|$. Using the identities for Ising type variables

$$\sigma_i \sigma_j = 2\delta_{\sigma_i \sigma_j} - 1, \quad \tau_i \tau_j = 2\delta_{\tau_i \tau_j} - 1, \quad (32)$$

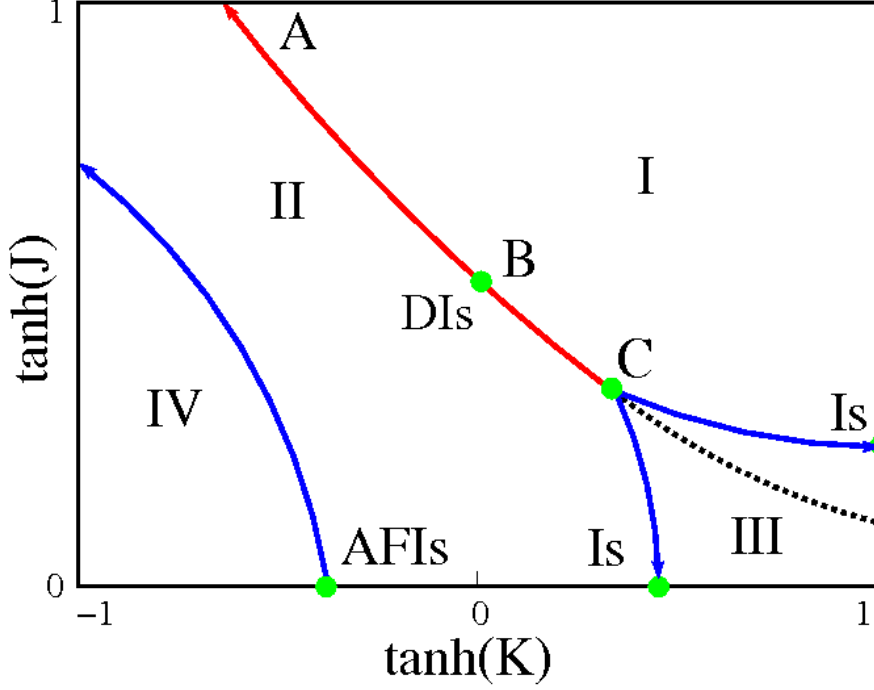


Figure 3. Phase diagram of the 2D symmetric Ashkin-Teller model defined by the Hamiltonian (28). The red ABC line is the self dual line. The point B at $K = 0$ corresponds to two uncoupled Ising models. The point C is the critical four-state Potts model at $K = J = (\log 3)/4$. At $J = 0$ there are two critical Ising points at $K = \pm(\log(1 + \sqrt{2}))/2$, one (Is) ferromagnetic and the other (AFIs) antiferromagnetic. For $K \rightarrow \infty$ there is another critical Ising point at $J = (\log(1 + \sqrt{2}))/2$. All continuous lines are critical. The blue lines $C - Is$ and the one starting at $AFIs$ are in the Ising universality class. The red line is critical with continuously varying critical exponents. The region denoted by I corresponds to a ferromagnetic phase for all the variables. In the region II, σ , τ , and $\sigma\tau$ are paramagnetic. In the region III only $\sigma\tau$ is ferromagnetic and in region IV $\sigma\tau$ exhibits antiferromagnetic order while σ and τ are paramagnetic.

we can rewrite Eq. (28) as

$$-H = J \sum_{\langle ij \rangle} (2\delta_{\sigma_i \sigma_j} + 2\delta_{\tau_i \tau_j} - 2) + K \sum_{\langle ij \rangle} (2\delta_{\sigma_i \sigma_j} - 1)(2\delta_{\tau_i \tau_j} - 1). \quad (33)$$

For convenience we shift the interaction (28) by $-4J$. In order to write the Boltzmann weight associated to a specific configuration we use $\exp(w\delta_{\sigma_i \sigma_j}) = (\exp(w) - 1)\delta_{\sigma_i \sigma_j} + 1$ and the analogous identity for the τ variables. The Boltzmann weight of a given link $\langle ij \rangle$ is then

$$\begin{aligned} \mathcal{W}_{\langle ij \rangle}(\sigma_i, \sigma_j, \tau_i, \tau_j) = & e^{-4J} + [e^{-2(J+K)} - e^{-4J}][\delta_{\sigma_i \sigma_j} + \delta_{\tau_i \tau_j}] + \\ & + [1 - 2e^{-2(J+K)} + e^{-4J}]\delta_{\sigma_i \sigma_j} \delta_{\tau_i \tau_j}. \end{aligned} \quad (34)$$

The key idea for the Swendsen-Wang algorithm is to introduce two new auxiliary Ising-type variables m_{ij} and n_{ij} living on the link $\langle ij \rangle$. We redefine the Boltzmann weight on the link $\langle ij \rangle$ as [48]

$$\mathcal{W}_{\langle ij \rangle}(\sigma_i, \sigma_j, \tau_i, \tau_j, m_{ij}, n_{ij}) = e^{-4J} \delta_{m_{ij} 0} \delta_{n_{ij} 0} +$$

$$\begin{aligned}
& + [e^{-2(J+K)} - e^{-4J}][\delta_{\sigma_i\sigma_j}\delta_{m_{ij}1}\delta_{n_{ij}0} + \delta_{\tau_i\tau_j}\delta_{m_{ij}0}\delta_{n_{ij}1}] + \\
& + [1 - 2e^{-2(J+K)} + e^{-4J}]\delta_{\sigma_i\sigma_j}\delta_{\tau_i\tau_j}\delta_{m_{ij}1}\delta_{n_{ij}1}.
\end{aligned} \tag{35}$$

Summing over m_{ij} and n_{ij} we obtain the weight in Eq. (34). Eq. (35) has a graphical interpretation in terms of clusters. In fact we can divide the links of the lattice in “activated” (if $m_{ij} = 1$) or “inactive” (if $m_{ij} = 0$). The same considerations hold for the n_{ij} variables. Therefore, each link of the lattice can be activated by setting $m_{ij} = 1$ or $n_{ij} = 1$. The active links connect different lattice sites forming clusters. There are clusters referring to the σ variables (called σ -clusters) and to the τ variables (τ -clusters). Isolated lattice sites are clusters as well. Obviously, the lattice sites belonging to the σ -clusters (τ -clusters) have the same value of σ (τ). The partition function of the extended model defined by the weight (35) can be written as

$$Z = \sum_{\sigma, \tau = \pm 1} \sum_{m, n = \pm 1} \prod_{\langle ij \rangle} \mathcal{W}_{\langle ij \rangle}(\sigma_i, \sigma_j, \tau_i, \tau_j, m_{ij}, n_{ij}). \tag{36}$$

We now proceed to the following definitions. We divide all the links into three classes: we define l_0 the total number of inactivated links; l_1 the total number of links connecting sites which belong only to one type of clusters either a σ -cluster or a τ -cluster. We define l_2 the total number of links on which m and n are both equal to 1. Furthermore we introduce the quantities

$$B_0 \equiv e^{-4J}, \tag{37}$$

$$B_1 \equiv [e^{-2(J+K)} - e^{-4J}], \tag{38}$$

$$B_2 \equiv [1 - 2e^{-2(J+K)} + e^{-4J}]. \tag{39}$$

The following step is to perform the summation over σ, τ in Eq. (35). This is readily done, obtaining the final expression for the partition function

$$Z = \sum_{\mathcal{C}\{\tau, \sigma\}} B_0^{l_0} B_1^{l_1} B_2^{l_2} 2^{C^\sigma + C^\tau}, \tag{40}$$

where we denoted with C^σ the number of σ -clusters and with C^τ the total number of τ -clusters. In the counting of τ -clusters (σ -clusters) we included all the lattice sites connected by a link on which $m_{ij} = 1$ ($n_{ij} = 1$). Isolated sites (with respect to m or n or both) count as single clusters. The links where $m_{ij} = 1, n_{ij} = 1$ contribute to both types of clusters.

3.2. Swendsen-Wang algorithm (the direct and embedded algorithms)

We are now in position to write the Swendsen-Wang algorithm for the symmetric AT model. The Monte-Carlo procedure can be divided in two steps. In the first one, given a configuration for (σ, τ) variables, we construct a configuration of the (m, n) variables. In the second step we update the (σ, τ) variables at given (m, n) . The details of the step one are

- if $\sigma_i = \sigma_j$ and $\tau_i = \tau_j$, we choose (m_{ij}, n_{ij}) with the following probabilities:
 - $(m_{ij}, n_{ij}) = (1, 1)$ with $p_1 = 1 - 2e^{-2(J+K)} + e^{-4J}$,
 - $(m_{ij}, n_{ij}) = (1, 0)$ with $p_2 = e^{-2(J+K)} + e^{-4J}$,
 - $(m_{ij}, n_{ij}) = (0, 1)$ with $p_2 = e^{-2(J+K)} + e^{-4J}$,
 - $(m_{ij}, n_{ij}) = (0, 0)$ with $p_3 = 1 - p_1 - 2p_2$,
- if $\sigma_i = \sigma_j$ and $\tau_i = -\tau_j$, the probabilities are
 - $(m_{ij}, n_{ij}) = (1, 0)$ with $p_1 = 1 - e^{-2(J-K)}$,

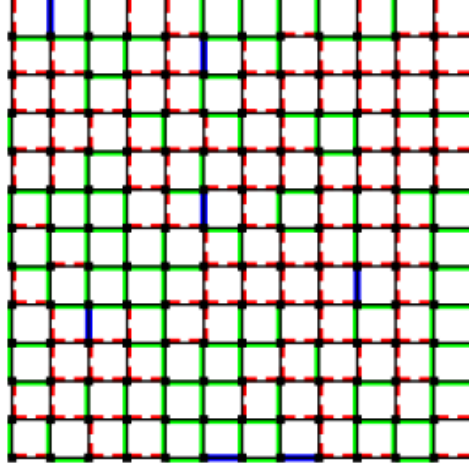


Figure 4. A typical cluster configuration on a 12×12 lattice. Green lines are σ -clusters and red dashed lines are τ -clusters. Links in blue are double links. Periodic boundary conditions on both directions are used.

- $(m_{ij}, n_{ij}) = (0, 0)$ with $p_2 = 1 - p_1$,
- if $\sigma_i = -\sigma_j$ and $\tau_i = \tau_j$, the probabilities are
 - $(m_{ij}, n_{ij}) = (1, 0)$ with $p_1 = 1 - e^{-2(J-K)}$,
 - $(m_{ij}, n_{ij}) = (0, 0)$ with $p_2 = 1 - p_1$,
- if $\sigma_i = -\sigma_j$ and $\tau_i = -\tau_j$ we choose $(m_{ij}, n_{ij}) = (0, 0)$ with probability 1.

In the step two, given the configuration of (m, n) generated using the rules above we build the connected σ -clusters and τ -clusters. The value of σ (τ) spins are required to be equal within each σ -cluster (τ -cluster). We choose randomly the spin value in each cluster and independently of the value assumed on the other clusters. This completes the update scheme. (Note a typo in Ref. [48]: the minus sign in step 2 and 3 of the update is missing.)

In Ref. [48] also the so called embedded version of the cluster algorithm is introduced. Its implementation is slightly easier compared to the direct algorithm. In the embedded algorithm instead of treating both σ and τ at the same time, one deals with only one variable per time. Let us consider the Boltzmann weight of a link $\langle ij \rangle$ at fixed configuration of τ

$$\mathcal{W}_{\langle ij \rangle}(\sigma_i, \sigma_j, \tau_i, \tau_j) = e^{-2(J+K\tau_i\tau_j)} + (1 - e^{-2(J+K\tau_i\tau_j)})\delta_{\sigma_i \sigma_j}. \quad (41)$$

The model defined by this weight can be simulated with a standard Swendsen-Wang algorithm for the Ising model using the effective coupling constant

$$J_{ij}^{eff} = J + K\tau_i\tau_j. \quad (42)$$

This is no longer translation invariant, but this does not affect the effectiveness of the cluster algorithm for the Ising model as long as $J_{ij}^{eff} \geq 0$. The same reasoning applies to the case of fixed σ . Thus, the embedded algorithm is made of two steps

- For a given configuration of τ variables, we apply a standard Swendsen-Wang algorithm to σ spins. The probability arising in the update step is $p_{ij} = 1 - e^{-2(J+K\tau_i\tau_j)}$.

- For a given configuration of σ variables, we update τ with the same algorithm and probability $p_{ij} = 1 - e^{-2(J+K\sigma_j\sigma_i)}$.

Direct and embedded algorithms are both extremely effective procedures to sample the AT configurations. However, very important for the following, Eq. (40) for the partition function does not hold anymore for a n -sheeted Riemann surface and we do not know whether it is possible to write the embedded algorithm for this case.

3.3. Rényi entanglement entropies via Monte Carlo simulation of a classical system.

In this section we summarize the method introduced by Caraglio and Gliozzi [18] to obtain the Rényi entropies via simulations of classical systems and we generalize it to the AT model. The partition function $Z = \text{Tr} e^{-\beta H}$ of a d -dimensional quantum system at inverse temperature β can be written as an Euclidean path integral in $d + 1$ dimensions [8]. Thus for the n -th power of the partition function one has

$$Z^n = \int \prod_{k=1}^n \mathcal{D}[\phi_k] e^{-\sum_{k=1}^n S(\phi_k)} \quad (43)$$

where $\phi_k \equiv \phi_k(\vec{x}, \tau)$ is a field living on the k -th replica of the system and $S(\phi_k)$ is the euclidean action (τ is the imaginary time.) The actual form of the action is not important, but for the sake of simplicity we restrict to the case of nearest-neighbor interactions

$$S(\phi_k) = \sum_{\langle ij \rangle} F(\phi_k(i), \phi_k(j)), \quad (44)$$

and the function F is arbitrary. We recall that $\text{Tr} \rho_A^n$ can be obtained by considering the euclidean partition function over a n -sheeted Riemann surface with branch cuts along the subsystem A [8]. (This equivalence is also the basis of all quantum Monte Carlo methods to simulate the block entanglement in any dimension [49].) Caraglio and Gliozzi constructed this n -sheeted Riemann surface for the lattice model in the following way. Let us consider a square lattice (for simplicity) and take the two points of its dual lattice surrounding A (that in 1+1 dimension is just an interval with two end-points). The straight line joining them defines the cut that we call λ . The length of λ is equal to the length of A . Let us consider n independent copies of this lattice with a cut. The n -sheeted Riemann lattice is defined by assuming that all the links of the k -th replica intersecting the cut connect with the next replica $k+1 \pmod n$. To get the partition function over the n sheeted Riemann surface we define the corresponding coupled action

$$S^n(\phi_k) = \sum_{k=1}^n \sum_{\langle ij \rangle \notin \lambda} F(\phi_k(i), \phi_k(j)) + \sum_{\langle ij \rangle \in \lambda} F(\phi_k(i), \phi_{k+1 \pmod n}(j)). \quad (45)$$

This definition can be used in any dimension, even though we will use here only $d = 2$. Finally, calling $Z_n(A)$ the partition function over the action (45), $\text{Tr} \rho_A^n$ is given by

$$\text{Tr} \rho_A^n = \frac{Z_n(A)}{Z^n}. \quad (46)$$

Following Ref. [18] we introduce the observable

$$\mathcal{O} \equiv e^{-S^n(\phi_1, \phi_2, \dots, \phi_n; \lambda) + \sum_{k=1}^n S(\phi_k; \lambda)}, \quad (47)$$

where S^n and S are the euclidean actions of the model defined on the n -sheeted lattice and on the n independent lattices respectively. The sum is restricted to links crossing the cut, as the presence of λ in the arguments stresses. It then follows

$$\langle \mathcal{O} \rangle_n \equiv \frac{Z_n(A)}{Z^n} = \text{Tr} \rho_A^n, \quad (48)$$

where $\langle \cdot \rangle_n$ stands for the average taken onto the uncoupled action $\sum_{k=1}^n S(\phi_k)$.

We can now discuss our improvement to the procedure highlighted so far. The practical implementation of Eq. (47) to calculate $\text{Tr} \rho_A^n$ is plagued by severe limitations: analyzing the Monte-Carlo evolution of the observable, one notices that it shows a huge variance because it is defined by an exponential. Direct application of Eq. (47) is possible then only for small lengths of the subsystem A . In order to overcome this problem, let us consider the quantity $Z_n(A)/Z^n$ and imagine to divide the subsystem in L parts to have $A = A_1 \cup A_2 \dots \cup A_L$, with the lengths of the various parts being arbitrary. Moreover we define a set of subsystems $\hat{A}_i \equiv \cup_{k=1}^i A_k$. Then it holds

$$\frac{Z_n(A)}{Z^n} = \prod_{i=0}^L \frac{Z_n(\hat{A}_{i+1})}{Z_n(\hat{A}_i)}. \quad (49)$$

Eq. (49) is very useful because each term in the product can be simulated effectively using a modified version of (47) if we choose the length of A_i to be small enough. In fact, by definition, we have

$$\langle \mathcal{O}(\hat{A}_i) \rangle_{\mathcal{R}_n(\hat{A}_i)} \equiv \frac{Z_n(\hat{A}_{i+1})}{Z_n(\hat{A}_i)}, \quad (50)$$

where $\mathcal{O}(\hat{A}_i)$ is the modified observable

$$\mathcal{O}(\hat{A}_i) \equiv \exp(-S^n(\hat{A}_{i+1}) + S^n(\hat{A}_i)). \quad (51)$$

We stress that in Eq. (50) the expectation value in the l.h.s must be taken on the coupled action on the Riemann surface with cut \hat{A}_i . The disadvantage of Eq. (49) is that, to simulate large subsystems, one has to perform L independent simulations and then build the observable taking the product of the results. If the dimension of each piece A_i is small this task requires a large computational effort. Another important aspect is the estimation of the Monte Carlo error: if each term in (49) is obtained independently, the error in the product is

$$\frac{\sigma(\mathcal{O})}{\overline{\mathcal{O}}} = \sqrt{\sum_{i=0}^L \frac{\sigma^2(\mathcal{O}(\hat{A}_i))}{\overline{\mathcal{O}(\hat{A}_i)}^2}}. \quad (52)$$

If the lengths of the intervals A_i are all equal, then the single terms of the summation in Eq. (52) do not change much and the total error should scale as \sqrt{L} .

Caraglio and Gliozzi [18] used another strategy to circumvent the problem with the observable in Eq. (47). The trick was to consider the Fortuin-Kastelaysn cluster expansion of the partition function of the Ising model. The analogous for the AT model was reported in the previous section

$$Z = \sum_{\mathcal{C}\{\sigma,\tau\}} B_0^{l_0} B_1^{l_1} B_2^{l_2} 2^{C^\sigma + C^\tau}, \quad (53)$$

where $\mathcal{C}^{\sigma,\tau}$ are the σ/τ -cluster configurations. Going from n independent sheets to the n -sheeted lattice, the type of links and their total number do not change, but the

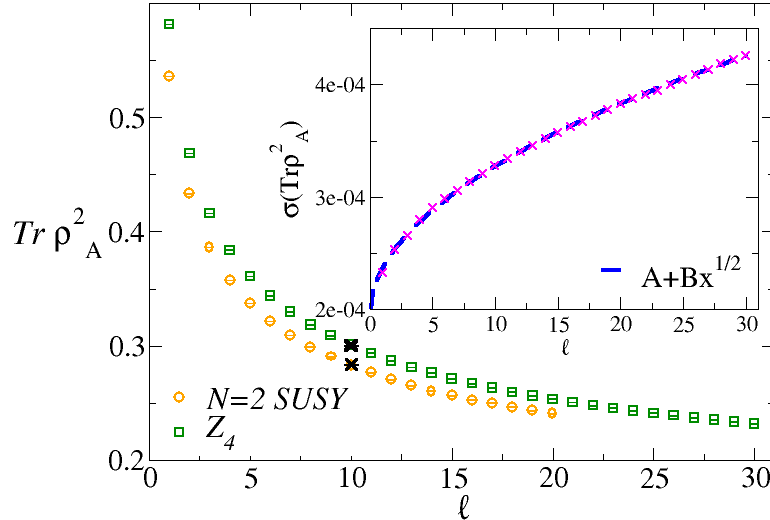


Figure 5. $\text{Tr} \rho_A^2$ for a single interval of length ℓ in a finite system of length $L = 120$. Data have been obtained by Monte Carlo simulations using the embedded algorithm. The orange points correspond to the SUSY model and the green ones to the Z_4 parafermions. The black crosses at $\ell = 10$ are data obtained using the direct algorithm. Inset: behavior of the statistical error of $\text{Tr} \rho_A^2$ vs ℓ for the SUSY model. The blue-dashed line is the expected form $A + B\ell^{1/2}$.

number of clusters does change, and so we get the cluster expression of observable (47) for the AT model

$$\mathcal{O}(\hat{A}_i) = 2^{[C_\sigma(\hat{A}_{i+1}) + C_\tau(\hat{A}_{i+1}) - C_\sigma(\hat{A}_i) - C_\tau(\hat{A}_i)]}, \quad (54)$$

where $C_\sigma(\hat{A}_i)$ ($C_\tau(\hat{A}_i)$) denote the total number of σ -clusters (τ -clusters) on the Riemann surface with cut \hat{A}_i . Since the clusters are non local objects, they represent “improved” observables and the variance for the Monte Carlo history of Eq. (54) is much smaller than in the naive implementation.

4. The entanglement entropy in the Ashkin-Teller model

4.1. The single interval

We first present the results for the Ashkin-Teller model for a single interval. Although these results do not provide any new information about the model, they are fundamental checks for the effectiveness of the Monte Carlo algorithms. We performed simulations using both algorithms described in the previous section: the direct cluster algorithm and the embedded one. When using the direct algorithm, measures are performed using the observable (54), while for the embedded algorithm we used the observable in Eq. (47). In Fig. 5 we report the results of the simulations of $\text{Tr} \rho_A^2$ for the SUSY model ($r_{\text{orb}} = \sqrt{3}/2$ in Fig. 1) and for the Z_4 parafermions ($r_{\text{orb}} = \sqrt{3}/2$) both for $L = 120$. The orange and green points are obtained using the embedded

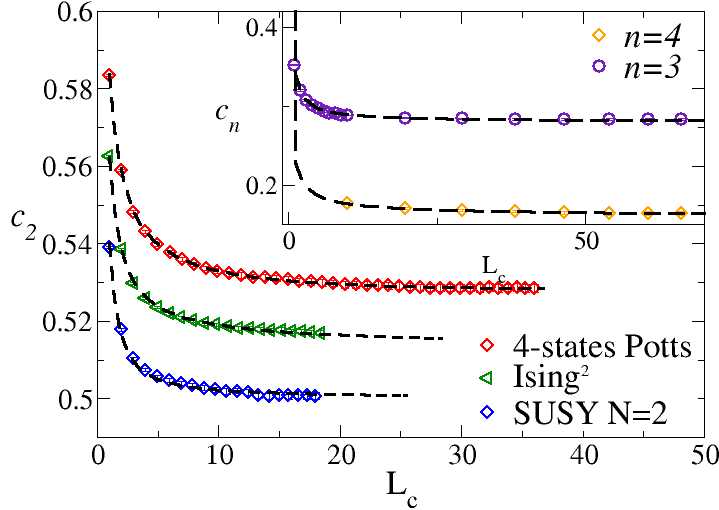


Figure 6. Plot of $c_2(L_c)$ as function of L_c for different ℓ and L . Three points on the self-dual line are reported: four-states Potts model, uncoupled Ising, and SUSY. The dashed lines are fits to the function $c_2 + BL_c^{-K_L}$ ($c_2 + AL_c^{-K_L} + BL_c^{-2K_L}$ for the 4-states Potts model) where K_L is $1/2, 1, 4/3$ respectively for the four-states Potts model, Ising, and SUSY. In the inset we report c_n for $n = 3, 4$ for the SUSY point. The dashed lines are fit to $A + BL_c^{2K_L/n}$, with $K_L = 4/3$ fixed.

algorithm. To check the implementation of the cluster observable, we report at $\ell = 10$ the data obtained using the direct algorithm and Eq. (54). The perfect agreement between the two results confirms the correctness of both implementations. Note that $\text{Tr} \rho_A^2$ is a monotonous function of ℓ , in contrast with the parity effects found for the XXZ spin chain [34, 35] that also corresponds to a vertex model [45]. In the inset we show the behavior of the statistical error of the observable (47) in the SUSY case as function of the subsystem length ℓ . It agrees with the prediction in Eq. (52) and its absolute value is extremely small, smaller than the size of the points in the main plot in Fig. 5. Analogous results have been obtained for all the critical points on the self-dual line using both algorithms.

The results for $\text{Tr} \rho_A^2$ in a finite system are asymptotically described by the CFT prediction (14) with $n = 2$ and $c = 1$. It is then natural to compute the ratio

$$c_2(L_c) = \frac{\text{Tr} \rho_A^2}{\left(\frac{L}{\pi} \sin\left(\frac{\pi}{L}\ell\right)\right)^{-1/4}}, \quad (55)$$

that is expected to be asymptotically a function of the chord-length $L_c = \left[\frac{L}{\pi} \sin\left(\frac{\pi}{L}\ell\right)\right]$. This allows to extract the non-universal quantity c_2 and to check the form of the corrections to the scaling. In Fig. 6 we report the results for $c_2(L_c)$ for the SUSY point, for the two uncoupled Ising models, and for the four states Potts model. It is evident that for large L_c , $c_2(L_c)$ approaches a constant value around 0.5. This is a first confirmation of the CFT predictions on the self-dual line.

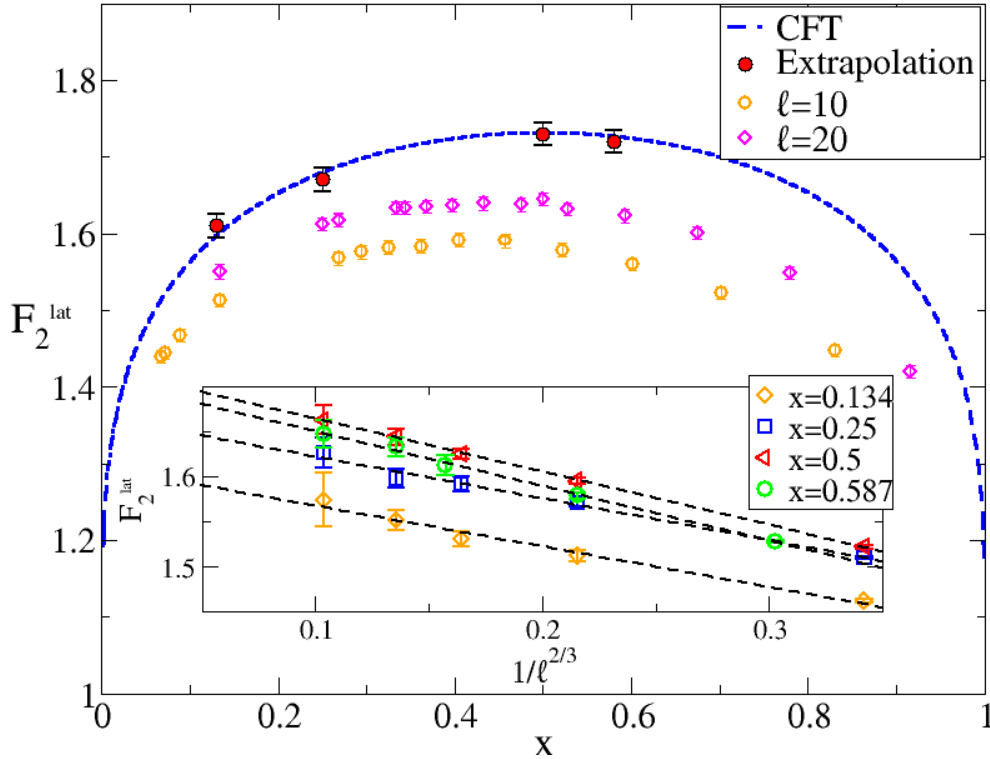


Figure 7. $F_2(x)$ versus the four point ratio x for the SUSY model. The red points are extrapolations obtained using the finite-size ansatz (57). The blue-dashed line is the *CFT* prediction. Inset: $F_2^{\text{lat}}(x)$ vs $1/\ell^{-2/3}$ for the four values of x used in the extrapolation ($x = 0.134, 0.25, 0.5, 0.587$). The dashed lines are fits to finite-size ansatz (57).

The previous results also provide a test for the theory of the corrections to the scaling to $S_A^{(n)}$. It has been shown [34, 35] that for gapless models described by a Luttinger liquid theory, the corrections to the scaling have the form $\ell^{-2K_L/n}$ (or $L_c^{-2K_L/n}$ for finite systems) where K_L is the Luttinger parameter, related to the circle compactification radius $K_L = 1/2\eta$. On the basis of general CFT arguments [36], it has been argued that this scenario is valid for any CFT and so also for the AT model with K_L replaced by the dimension of a proper operator. It is then natural to expect that for the AT model this dimension is K_L in Eq. (31), also on the basis of the results for the Ising model [34, 50]. The dashed lines in Fig. 6 are fits of $c_2(L_c)$ with the function $c_2 + AL_c^{-K_L}$. The agreement is always very good, except for the four-state Potts model, for which the exponent of the leading correction K_L assumes the smallest value and so subleading corrections enter (as elsewhere in similar circumstances, see e.g. [35]). In fact, the fit with the function $c_2 + AL_c^{-K_L} + BL_c^{-2K_L}$ is in perfect agreement with the data (but the presence of another fit parameter makes this result not so robust). This analysis confirms that K_L is the right exponent governing the corrections to the scaling.

In the inset of Fig. 6 we also report the values of c_n for $n = 3, 4$ as a function of L_c . c_n becomes smaller as n increases as for the *XXZ* [34], *XX* [51], and *Ising* [50, 52]

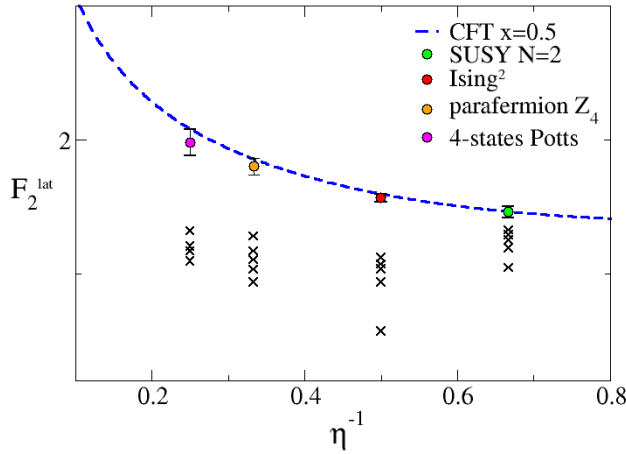


Figure 8. $F_2^{\text{lat}}(1/2)$ as function of η^{-1} for different models (Ising, SUSY, Z_4 parafermions, and four-states Potts model). The blue-dashed line is the CFT prediction. The (colored) points close to the curve are extrapolations obtained with the finite-size scaling ansatz (57). The black crosses are the Monte Carlo data used for the fits. The block lengths used range from $\ell = 5$ to $\ell = 80$.

spin-chains. The dashed lines are fits to the expected scaling behavior $L_c^{-2K_L/n}$ of the corrections, that reproduce perfectly the data.

4.2. The entanglement entropy of two disjoint intervals.

In this section we investigate the entanglement entropy of two disjoint intervals and check the correctness of our prediction (25) for the AT model on the self-dual line. As for all other cases studied so far numerically (i.e. Heisenberg [17], Ising [24, 26], and XY [26] chains), strong scaling corrections affect the determination of the scaling function $F_n(x)$. CFT predictions have been confirmed only using the general theory of corrections to the scaling [34, 35, 36, 37].

In order to determine the function $F_n(x)$, we consider the ratio

$$F_n^{\text{lat}}(x) = \frac{\text{Tr} \rho_{A_1 \cup A_2}^n}{\text{Tr} \rho_{A_1}^n \text{Tr} \rho_{A_2}^n} (1-x)^{c(n-1/n)/6}, \quad (56)$$

and, on the basis of the general CFT arguments [36], we expect that the the leading correction to scaling can be effectively taken into account by the scaling ansatz

$$F_n^{\text{lat}}(x) = F_n^{\text{CFT}}(x) + \ell^{-2\omega/n} f_n(x) + \dots \quad (57)$$

For the Ising model it has been found $\omega = 1/2$ [24, 26]. Since for $\eta = 2$ the AT Hamiltonian reduces to two uncoupled Ising models, one naively expects $\omega = K_L/2$ along the whole self-dual critical line of the AT model.

Hereafter we only consider $\text{Tr} \rho_A^2$. We start our analysis from the SUSY point that (assuming $\omega = K_L/2$) should have the smaller corrections to scaling. In Fig. 7 we show Monte Carlo data at $\ell = 10, 20$ ($L = 120$) for $F_2^{\text{lat}}(x)$ plotted against the four point ratio x defined as in Eq. (15). We report with the blue dashed line the

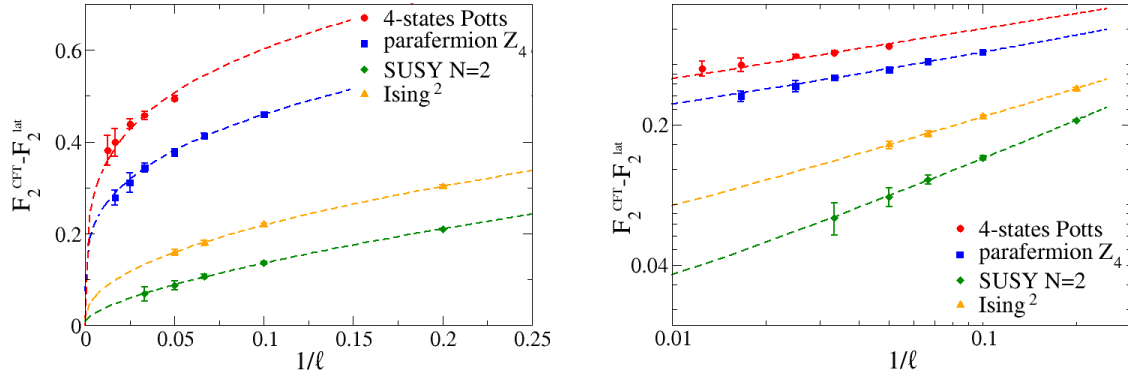


Figure 9. $F_2^{\text{CFT}}(1/2) - F_2^{\text{lat}}(1/2)$ versus $1/\ell$. The dashed lines are fits to the finite-size scaling ansatz (57) fixing the value of $F_2^{\text{CFT}}(1/2)$. Left: the same plot in log-log scale.

asymptotic CFT result (cf. Eq. (25)). As in all other cases considered in the literature [24, 26], the curves for $F_2(x)$ at $\ell = 10, 20$ are not symmetric functions of $x \rightarrow 1 - x$, as instead the asymptotic CFT prediction must always be [17]. This is due to the non-symmetrical finite-size corrections $f_2(x)$ in Eq. (57). We extrapolate the result at $\ell \rightarrow \infty$ using the ansatz (57) and $\omega = 2/3$. The extrapolations are reported as red points in Fig. 7. There is a very good agreement between the extrapolations and the theoretical curve. Since the correction exponent $\omega = 2/3$ is rather large, and so the corrections small, even small subsystems such as $\ell = 10, 20$ are enough to obtain a good extrapolation. In the inset of Fig. 7 we report the Monte Carlo data for $F_2^{\text{lat}}(x)$ against $\ell^{-2/3}$. The linear behavior in this inset confirms the validity of the ansatz (57) and the reported straight lines are the fits giving the extrapolations reported in the main panel.

We also investigate other points on the self dual line, namely the 4-states Potts model ($\eta = 4$), the parafermion Z_4 ($\eta = 3$), the uncoupled Isings ($\eta = 2$). In Fig. 8 we report $F_2^{\text{lat}}(x) - F_2^{\text{CFT}}(x)$ at fixed $x = 1/2$ versus η^{-1} for all the mentioned models. we report $x = 1/2$ because it is the value of x providing the most stable estimate, but also other values have been studied. Indeed, on one hand, the computational cost of the simulations decreases going toward $x = 1$ (the reason being evident from the definition of x for which smaller lattice sizes are needed). On the other hand, scaling corrections become more severe in the region $x \sim 1$, as clear from the results for the SUSY model in Fig. 7. Thus $x = 1/2$ represents the best compromise between these two drawbacks. The dashed curves in the left panel of Fig. 9 are fits to the data with Eq. (57) obtained by fixing the value of $F_2^{\text{CFT}}(x)$ to its predicted value (cf. Eq. (25)). There is a very good agreement with the full theoretical picture, confirming in particular the correctness of the exponent governing the leading correction to the scaling. For the Z_4 parafermions and for the four-state Potts model, we needed very large values of ℓ in order to show the correct asymptotic behavior (the range of ℓ reported in the plot is in fact $5 \leq \ell \leq 80$). This is made clearer in the right panel of Fig. 9 where the same data are shown in log-log scale. In Fig. 8 we reports the

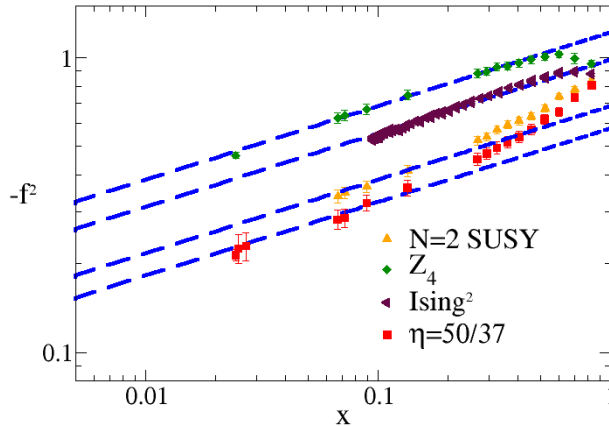


Figure 10. Monte Carlo data for $f_2(x)$ obtained as $f_2(x) = (F_2^{\text{lat}}(x) - F_2^{\text{CFT}}(x))\ell^{K_L/2}$ as function of x . We show data for $\ell = 10$ and various models (SUSY, Z_4 parafermions, Ising model and the model corresponding to $\eta^{-1} = 0.74$). The blue-dashed lines are asymptotic fits to $Ax^{1/4}$.

fits obtained by fixing only the exponent of the corrections $\omega = K_L/2$ and leaving $F_2^{\text{CFT}}(1/2)$ free. For all considered values of η , the extrapolation of $F_2^{\text{lat}}(1/2)$ to $\ell \rightarrow \infty$ is compatible (within error bars) with the expected result $F_2^{\text{CFT}}(1/2)$.

We finally study the correction amplitude $f_2(x)$ in Eq. (57). This function is the main reason of the asymmetry in $x \rightarrow 1 - x$ for $F_2^{\text{lat}}(x)$ and knowing its gross features could greatly simplify future analyses. For the Ising model, it has been found that $f_2(x) \sim x^{1/4}$ for small x , that is the same behavior of $F_2(x) - 1$. Since along the whole self-dual line $F_2(x) - 1 \sim x^{1/4}$, we would expect

$$f_2(x) \sim x^{1/4}. \quad (58)$$

For the Ising model (i.e. $\eta = 2$), this scenario has been already verified with high precision [24].

In Fig. 10 we report $f_2(x)$ obtained as $f_2(x) = (F_2^{\text{CFT}}(x) - F_2^{\text{lat}}(x))\ell^{K_L/2}$ as function of x (in logarithmic scale to highlight the small x behavior). All data correspond to $\ell = 10$ and various values of L . For the two largest values of η (Z_4 parafermionic theory at $\eta = 3$ and for the Ising model at $\eta = 2$), we observe an excellent agreement with our conjecture $f_2(x) \sim x^{1/4}$. However decreasing the value of η , i.e. for the SUSY model at $\eta = 3/2$ and for the model at $\eta^{-1} = 0.74$, the behavior of $f_2(x)$ is not as linear as before, especially for high value of x . Nonetheless for $x < 0.4$ the data confirm the behavior $x^{1/4}$. Furthermore, it seems that for any $\eta \neq 2$, subleading terms in the expansion for small x appear and they are vanishing only for the Ising model.

5. The Tree Tensor Network

This section is divided into two parts. First we explain in a self contained way how to extract the spectrum of the reduced density matrix of some specific bipartitions

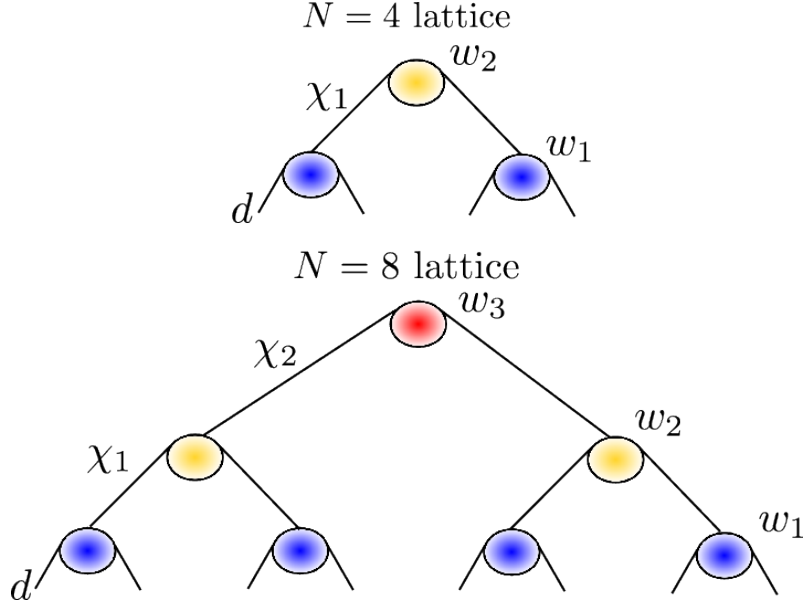


Figure 11. Examples of TTN for a $N = 4$ lattice and a $N = 8$ lattice.

of a pure state encoded in a Tree Tensor Network (TTN). We only recall the basic definitions introduced in Ref. [53] and refer the reader to the literature for complementary works on the subject [54, 55, 56, 57, 58, 59, 60, 61, 62, 63, 64, 65, 66]. Secondly we quickly recall how to use TTN to calculate the ground state of the anisotropic Heisenberg spin-chain.

5.1. Tree Tensor network and reduced density matrices.

We consider a one dimensional lattice \mathcal{L} made of N sites, where each site is described by a local Hilbert space \mathbf{V} of finite dimension d . In this work the state is the ground state $|\Psi_{\text{GS}}\rangle$ of some local Hamiltonian H defined on \mathcal{L} , but in general it could be an arbitrary pure state $|\Psi\rangle \in \mathbf{V}^{\otimes N}$ defined on the lattice \mathcal{L} .

A generic state $|\Psi\rangle \in \mathbf{V}^{\otimes N}$ can always be expanded as

$$|\Psi\rangle = \sum_{i_1=1}^d \sum_{i_2=1}^d \cdots \sum_{i_N=1}^d T_{i_1 i_2 \cdots i_N} |i_1\rangle |i_2\rangle \cdots |i_N\rangle, \quad (59)$$

where the d^N coefficients $T_{i_1 i_2 \cdots i_N}$ are complex numbers and the vectors $\{|1_s\rangle, |2_s\rangle, \cdots, |d_s\rangle\}$ denote a local basis on the site $s \in \mathcal{L}$. We refer to the index i_s that labels a local basis for site s ($i_s = 1, \cdots, d$) as a *physical* index.

In the case we are interested in, the tensor of coefficients $T_{i_1 i_2 \cdots i_N}$ in Eq. (59) is the result of the contraction of a TTN. As shown in Fig. 11 for lattices of $N = 4$ and $N = 8$ sites, a TTN decomposition of $T_{i_1 i_2 \cdots i_N}$ consists of a collection of tensors w that have both *bond* indices and *physical* indices. The tensors are interconnected by the bond indices according to a tree pattern. The N physical indices correspond to the leaves of the tree. Upon summing over all the bond indices, the TTN produces the d^N complex coefficients $T_{i_1 i_2 \cdots i_N}$ of Eq. (59).

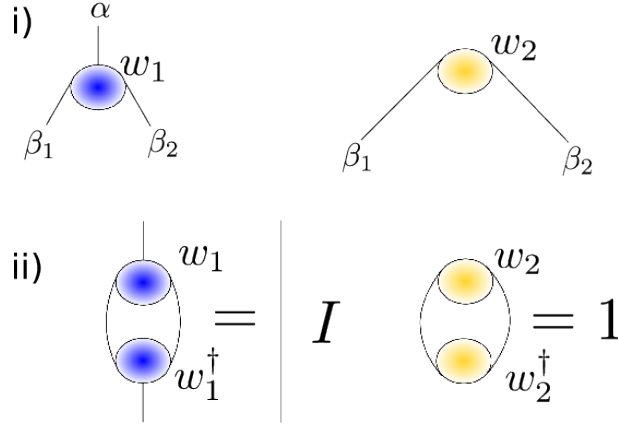


Figure 12. (i) Diagrammatic representation of the two types of isometric tensors in the TTN for a $N = 4$ lattice in Fig. 11. (ii) Graphical representation of the constraints in Eqs. (61) and (62) fulfilled by the isometric tensors.

The tensors in the TTN will be constrained to be *isometric*, in the following sense. As shown in Fig. 12 for the $N = 4$ lattice of Fig. 11, each tensor w in a TTN has at most one upper leg/index α and two lower indices/legs β_1, β_2 , so that its entries read $(w)_{\beta_1, \beta_2}^\alpha$ (everything can be generalized to tensors with more upper and lower legs [53]). Then we impose that

$$\sum_{\beta_1, \beta_2} (w)_{\beta_1, \beta_2}^\alpha (w^\dagger)_{\alpha'}^{\beta_1, \beta_2} = \delta_{\alpha\alpha'}. \quad (60)$$

For clarity, throughout this paper we use diagrams to represent tensors networks as well as tensor manipulations. For instance, the constraints for the tensors w_1 and w_2 of the TTN of Fig. 11 for a $N = 4$ lattice, namely

$$\sum_{\beta_1, \beta_2} (w_1)_{\beta_1, \beta_2}^\alpha (w_1^\dagger)_{\alpha'}^{\beta_1, \beta_2} = \delta_{\alpha\alpha'}, \quad (61)$$

$$\sum_{\beta_1, \beta_2} (w_2)_{\beta_1, \beta_2} (w_2^\dagger)^{\beta_1, \beta_2} = 1, \quad (62)$$

are represented as the diagrams in Fig. 12(ii). We refer to a tensor w that fulfills Eq. (60) as an *isometry*.

An intuitive interpretation of the use of a TTN to represent a state $|\Psi\rangle$ can be obtained in terms of a coarse-graining transformation for the lattice \mathcal{L} . Notice that the isometries w in Fig. 11 are organized in layers. The bond indices between two layers can be interpreted as defining the sites of an effective lattice. In other words, the TTN defines a sequence of increasingly coarser lattices $\{\mathcal{L}_0, \mathcal{L}_1, \dots, \mathcal{L}_{T-1}\}$, where $\mathcal{L}_0 \equiv \mathcal{L}$ and each site of lattice \mathcal{L}_τ is defined in terms of several sites of $\mathcal{L}_{\tau-1}$ by means of an isometry w_τ , see Fig. 13. In this picture, a site of the lattice \mathcal{L}_τ effectively corresponds to some number n_τ of sites of the original lattice \mathcal{L}_0 . For instance, each of the two sites of \mathcal{L}_2 in Fig. 13 corresponds to 8 sites of \mathcal{L}_0 . Similarly, each site of lattice \mathcal{L}_1 corresponds to 4 sites of \mathcal{L}_0 .

The use of isometric tensors, and the fact that each bond unambiguously defines two parts ($A : B$) of the chain which are connected only through that bond as displayed

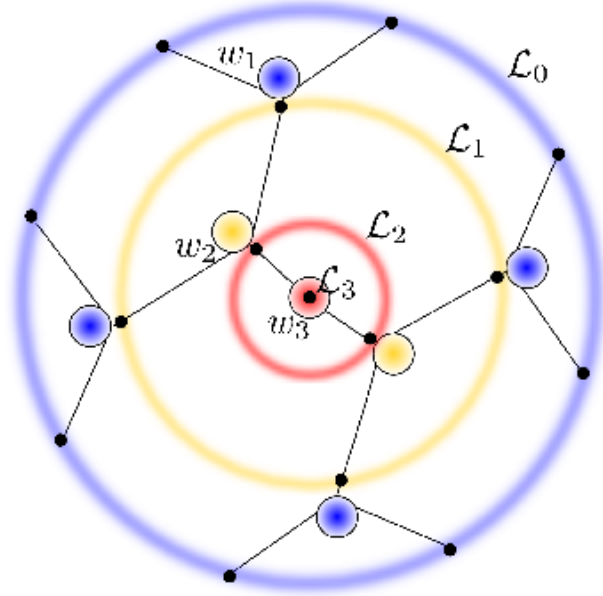


Figure 13. The isometric TTN of Fig. 11 for a $N = 8$ lattice \mathcal{L}_0 with periodic boundary conditions (the blue external circle) is associated with a coarse-graining transformation that generates a sequence of increasingly coarse-grained lattices \mathcal{L}_1 , \mathcal{L}_2 and \mathcal{L}_3 (the inner circles). Notice that in this example we have added an extra index to the top isometry w_3 , corresponding to the single site of an extra top lattice \mathcal{L}_3 , which we can use to encode in the TTN a whole subspace of $\mathbf{V}^{\otimes N}$ instead of a single state $|\Psi\rangle$.

in Fig. 14, implies that the rank of that bond in the TTN is given by the Schmidt rank $\chi(A : B)$ of the partition $(A : B)$ [59]. Thus the reduced density matrix ρ_A for a set A of sites of \mathcal{L} is

$$\rho_A = \text{tr}_B |\Psi\rangle\langle\Psi| = \sum_{\alpha} p_{\alpha} |\Psi_{\alpha}^A\rangle\langle\Psi_{\alpha}^A|, \quad (63)$$

where p_{α} are the eigenvalues of ρ_A . It follows then the Rényi entanglement entropies $S_A^{(n)}$ are

$$S_A^{(n)} = \frac{1}{1-n} \log \text{Tr} \rho_A^n = \frac{1}{1-n} \log \sum_{\alpha} p_{\alpha}^n, \quad (64)$$

and for $n = 1$

$$S_A^{(1)} = -\text{tr}(\rho_A \log \rho_A) = -\sum_{\alpha} p_{\alpha} \log p_{\alpha}. \quad (65)$$

In the following we denote the ranks of the tensor w_{τ} , α, β_1, β_2 as $\chi^{\tau}, \chi^{\tau-1}, \chi^{\tau-1}$. In general, they fulfill

$$\chi^{\tau} < (\chi^{\tau-1})^2, \quad (66)$$

meaning that w_{τ} projects states in $\mathbf{V}^{\tau-1} \otimes \mathbf{V}^{\tau-1}$ into the smaller Hilbert space \mathbf{V}^{τ} .

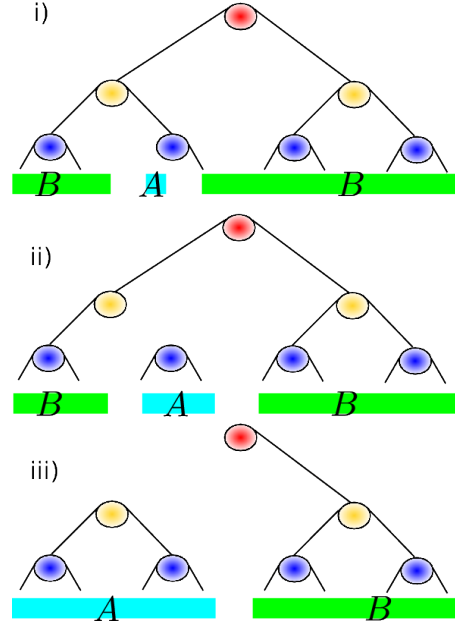


Figure 14. By erasing one of the indices in the TTN the spin chain is always divided in two parts A and B [59]. Here we show that in the case of the $N = 8$ lattice of Fig. 11 there are three classes of indices, identified by their position in the TTN. i) physical bonds connect a single spin with the rest of the lattice, ii) bond indices of the first layer connect a block of two adjacent spins to the rest of the lattice, iii) bond indices of the third layer of the lattice connect four adjacent spins, to the other half. This implies that the rank of the index is the Schmidt rank of the respective partition.

For a critical chain, the logarithmic scaling of the entanglement entropy (cf. Eq. (2)) implies that the rank of the isometries should at least grow proportionally to the length of the block represented by the effective spins

$$\chi^\tau \propto n_\tau, \quad (67)$$

which means that while moving to higher layer of the tensor network the rank of the isometries increases. This also implies that the leading cost of the computation is concentrated in contracting the first few layers of the TTN. If $N = 2^T$ and we describe a pure state (so that the rank of the α_τ is one) the maximal rank of the tensors in the TTN is

$$\chi = \max_\tau \chi^\tau = \chi^{T-1}. \quad (68)$$

In Ref. [53] it has been shown that i) a TTN description of the ground state of chain of length N with periodic boundary conditions can be obtained numerically with a cost of order $\mathcal{O}(\log N \chi^4)$. ii) From the TTN it is also straightforward to compute the spectrum $\{p_\alpha\}$ of the reduced density matrix ρ_A (cf. Eq. (63)) when A is a block of contiguous sites corresponding to an effective site of any of the coarse-grained lattices $\mathcal{L}_1, \dots, \mathcal{L}_{T-1}$. Fig. 15 illustrates the tensor network corresponding to ρ_A for the case when A is one half of the chain. Many pairs of isometries are annihilated. In addition, the isometries contained within region A can be removed since they do

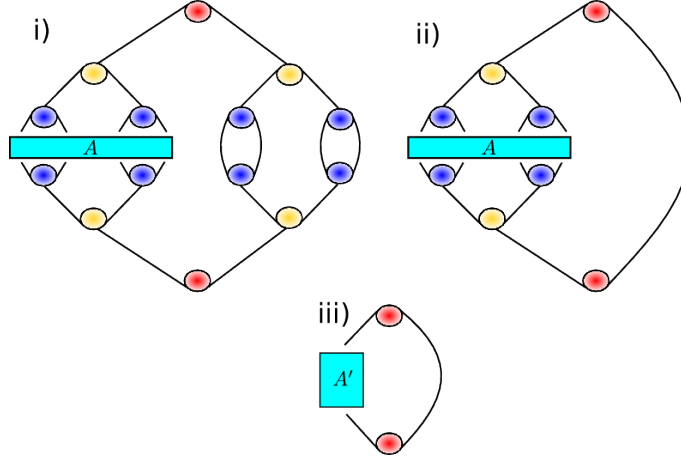


Figure 15. Computation of the spectrum $\{p_\alpha\}$ of the reduced density matrix ρ_A for a block A that corresponds to one of the coarse-grained sites. (i) Tensor network corresponding to ρ_A where A is half of the lattice. (ii) Tensor network left after several isometries are annihilated with their Hermitian conjugate. (iii) since the spectrum of ρ_A is not changed by the isometries acting on A , we can eliminate them and we are left with a network consisting of only two tensors, which can now be contracted together. The cost of this computation is proportional to $\mathcal{O}(\chi'^3\chi^2) \leq \mathcal{O}(\chi^5)$.

not affect the spectrum of ρ_A . From the spectrum $\{p_\alpha\}$, we can now obtain the Rényi entropies $S_A^{(n)}$. The leading cost for computing the spectrum of the reduced density matrix ρ_A for this class of bipartitions is due to the contractions of the first layers of the TTN. When the bipartition is such that A is a quarter of the chain, this implies a cost proportional to $\mathcal{O}(\chi'^3\chi^2) \leq \chi'\chi^4$, where $\chi' = \chi^{T-2}$.

It is also possible to compute the reduced density matrix ρ_A when A is composed of two disjoint subintervals A_1 and A_2 , where now each of the two intervals is a block of contiguous sites corresponding to an effective site of the coarse grained lattice. The cost of this computation is again dominated by contracting the upper part of the tensor network, and the most expensive case is obtained by considering A as the collection of two $N/4$ spins blocks, separated by $N/4$ spins. The tensor network corresponding to this ρ_A is shown in Fig. 16. Also in this case many pairs of isometries are annihilated. The isometries contained within the composed region A can also be removed since they do not affect the spectrum of ρ_A . The cost of contracting this tensor network is proportional to $\max[\mathcal{O}(\chi^2\chi'^4), \mathcal{O}(\chi^3\chi'^2)] < \mathcal{O}(\chi^6)$.

5.2. The TTN and the anisotropic Heisenberg spin-chain

In the previous subsection we have shown how to extract the spectrum of the reduced density matrix for a single and a double spin block from a TTN state. In this manuscript we are interested in reduced density matrices calculated on the ground-state of the anisotropic Heisenberg spin chain (XXZ model) in zero magnetic field,

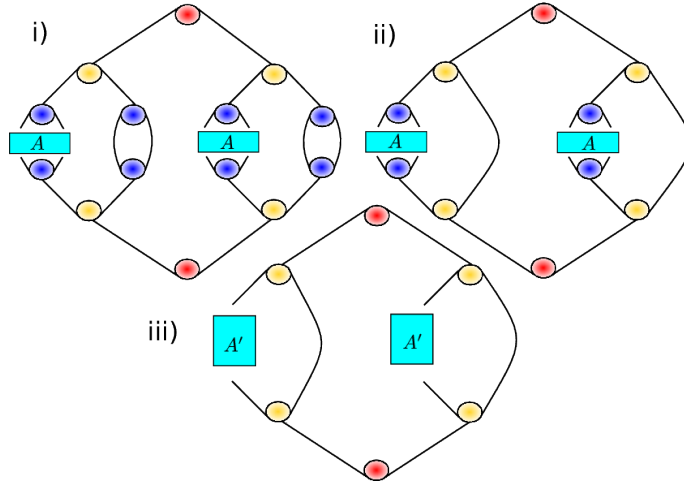


Figure 16. Computation of the spectrum $\{p_\alpha\}$ of the reduced density matrix ρ_A when A corresponds to two coarse-grained sites separated by one coarse grained site from both sides. (i) Tensor network corresponding to ρ_A where A is a quarter of the lattice. (ii) Tensor network left after several isometries are annihilated with their Hermitian conjugate. (iii) Since the spectrum of ρ_A is not changed by the isometries acting on A , we can eliminate them and we are left with a network consisting of only few tensors, which can now be contracted together. The cost of contracting this tensor network is proportional to $\max[\mathcal{O}(\chi^2\chi'^4), \mathcal{O}(\chi^3\chi'^2)] < \mathcal{O}(\chi^6)$.

defined by the Hamiltonian

$$H = \sum_{j=1}^L [\sigma_j^x \sigma_{j+1}^x + \sigma_j^y \sigma_{j+1}^y + \Delta \sigma_j^z \sigma_{j+1}^z], \quad (69)$$

where σ_j^α are the Pauli matrices at the site j . Periodic boundary conditions are assumed. We are interested in gapless conformal phases of the model, that is $-1 < \Delta \leq 1$. This phase is described by a free-bosonic CFT compactified on a circle with radius that depends on the parameter Δ

$$\eta = 2r_{\text{circle}}^2 = \frac{1}{2K_L} = \frac{\arccos(-\Delta)}{\pi}, \quad (70)$$

where K_L is the Luttinger liquid parameter. § The sign convention in the Hamiltonian (69) is such that the model is (anti)ferromagnetic for $\Delta < 0$ ($\Delta > 0$). Hamiltonian (69) is diagonalizable by means of Bethe ansatz. However, obtaining the spectrum of the reduced density matrix from Bethe ansatz is still a major problem and only results for small subsystems are known [44, 67]. For this reason we exploit variational TTN techniques to obtain the ground state.

Here we follow the variational procedure described in detail in Ref. [53], where the generic technique (consisting of assuming a tensor network description of the ground state and minimize the energy variationally improving the tensors one by one as described, i.e., in Ref. [4]) has been specialized and optimized for the case of a

§ Notice similarities and differences between Eq. (70) and its analogous for the AT model (31). The relation between η and r^2 and the relation between K_L and Δ are the same for both XXZ spin-chain and AT model, but the relation between η and Δ (or K_L and r) is different.

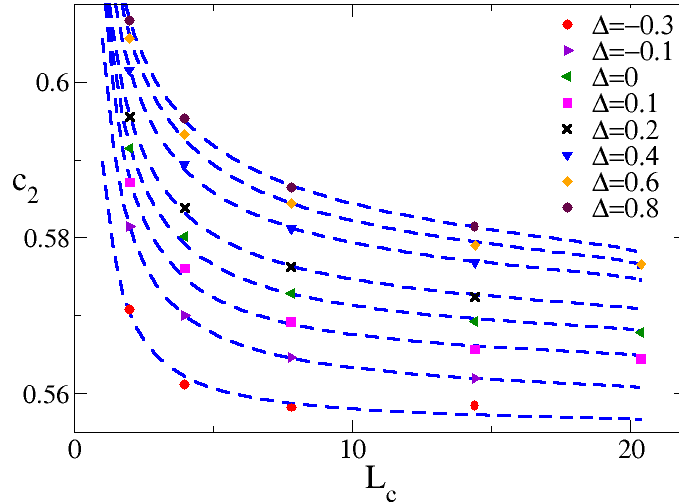


Figure 17. TTN data for the non universal constant $c_2(L_c)$ as function of the chord length L_c for different values of Δ . The dashed curves are fits to the function $A + BL_c^{-KL}$. The reported data have been obtained with $L = 128$ for $\Delta = 0, 0.1, 0.6$ and $L = 64$ for the other values.

TTN. We exploit translation invariance by using the same tensor at each layer of the TTN. One could also improve the efficiency further by exploiting the $U(1)$ symmetry of the Hamiltonian (69), i.e. the rotations around the z axis. However we did not make use of this symmetry here.

6. The Block Entanglement of the Anisotropic Heisenberg spin-chain

In this section we report the TTN results for the Rènyi entropies in the XXZ spin-chain for a single and a double interval. As a main advantage compared to the classical Monte Carlo simulations performed for the AT model, with a single TTN simulation we obtain the spectrum of the reduced density matrix and hence any Rènyi entropy, including von Neumann $S_A^{(1)}$. Oppositely with the Monte Carlo methods only Rènyi entropies $S_A^{(n)}$ of integer order $n \geq 2$ can be obtained and each of them requires an independent simulation.

6.1. The single interval.

We first present the TTN results for the single interval. These have been already obtained with many numerical variational techniques [34, 68, 69, 38] and are reported here only to test the accuracy of the TTN and to fix units/scales etc. Using variational TTN, we find the ground-state of the XXZ Hamiltonian (69) and from this we extract the spectrum of the reduced density matrix of the single block, as explained in the previous section. We then numerically obtain $\text{Tr} \rho_A^n$. The maximum size of the chain

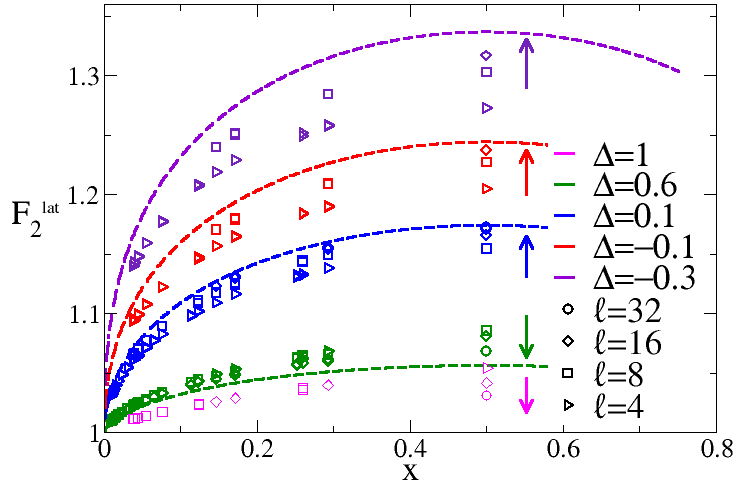


Figure 18. TTN data for $F_2^{\text{lat}}(x)$ as function of x for various sizes of the chain $L = 16, 32, 64, 128$, subsystem lengths $\ell = 4, 8, 16, 32$, and $\Delta = -0.3, -0.1, 0.1, 0.6$. Different values of Δ are distinguished by different colors, while different symbols denote different values of ℓ . The arrows denote the (asymptotically) increasing subsystem sizes ℓ .

that we consider is $L = 128$. The subsystem lengths considered are $\ell = 2, 4, 8, 16, 32$. Notice that with the TTN method, using a binary tree as we are doing, we can effectively access only subsystems sizes of the form 2^m with m arbitrary integer, as it should be clear from the previous section. In particular this limits the calculation to even values of ℓ and we can not study the parity effects reported in Ref. [34, 35].

We considered different values of the anisotropy parameter Δ , namely $\Delta = -0.3, -0.1, 0, 0.1, 0.2, 0.4, 0.6, 0.8, 1$. The TTN becomes less effective for values of $\Delta \leq -0.5$. This can be easily traced back to the smallness of the finite-size gap that in the minimization process causes the algorithm to be stuck in meta-stable states when the system size is large enough. This drawback could be cured by using larger values of χ (and so larger computational cost), but as we shall see, the considered values of Δ suffice to draw a very general picture of the entanglement. For the isotropic Heisenberg antiferromagnet at $\Delta = 1$ we ignore the presence of logarithmic corrections to the scaling [68, 36], that have a minimal effect for all our aims.

As for the AT model, we study the quantity $c_2(L_c)$ defined by the ratio in Eq. (55). The results are shown in Fig. 17 for all considered values of Δ . The scaling corrections are evident, especially for larger values of Δ , as expected [34]. These corrections for $\text{Tr}\rho_A^n$ are indeed of the form $L_c^{-2K_L/n}$ [34] (K_L is defined in Eq. (70)). The dashed lines reported in Fig. 17 are fits to this form for $n = 2$, showing the agreement between TTN data and the fits. We checked that all the TTN data agree with the ones obtained in Ref. [34] using density matrix renormalization group. The agreement is perfect and for this reason we refer to the above paper for a detailed

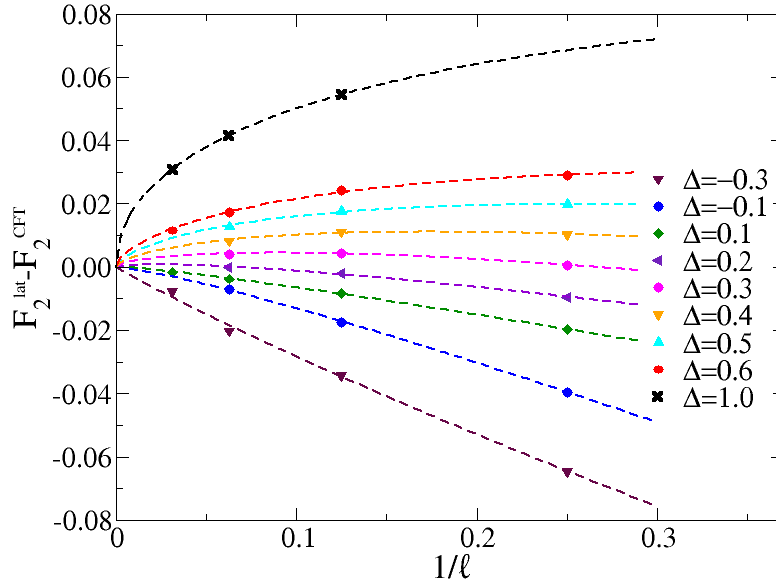


Figure 19. TTN data for $F_2^{\text{lat}}(1/2) - F_2^{\text{CFT}}(1/2)$ as function of $1/\ell$ for various Δ . The dashed lines are fits to the function with the generalized finite- ℓ ansatz (71).

study of $\text{Tr} \rho_A^n$ for $n > 2$.

6.2. Double interval: the $n = 2$ case.

We now consider a subsystem made of two parts A_1 and A_2 of equal length ℓ . We start by studying the quantity $\text{Tr} \rho_{A_1 \cup A_2}^2$ for finite chains and extract the universal function $F_2^{\text{CFT}}(x)$ by proper extrapolation. Since we only consider even ℓ , corrections to the scaling are expected to be monotonic in ℓ also for $F_2(x)$, oppositely to the case of arbitrary ℓ parity [17, 26]. The CFT prediction for the function $F_2(x)$ for the XXZ chain is Eq. (5) with η given by Eq. (70).

In Fig. 18 we report TTN data for $F_2^{\text{lat}}(x)$ (obtained with the ratio defined in Eq. (56)) as function of the cross ratio x for $\Delta = -0.3, -0.1, 0.1, 0.6$ and subsystem sizes $\ell = 4, 8, 16, 32$. The different values of Δ are denoted with different colors, while the different symbols stand for the various ℓ . On the same figure we also show the asymptotic $F_2^{\text{CFT}}(x)$ as dashed lines. It is evident that strong scaling corrections affect the data, as expected. Colored arrows denote the direction of (asymptotically) increasing subsystem sizes. Very surprisingly, while for $\Delta = -0.3, -0.1, 0.1$ the asymptotic CFT result is approached from below, for $\Delta = 0.6$ it is approached from above. Moreover, for $\Delta = 0.6$ the behavior of the data is not monotonic. This contrasts the results obtained for the AT model in the previous sections and the ones obtained for the XX and Ising spin-chains [26].

In order to shed some light on this unexpected phenomenon, it is worth to look at $F_2^{\text{lat}}(x)$ as functions of ℓ for fixed values of x . In Fig. 19 we report one of these plots for $x = 1/2$. Analogous figures are obtained for other values of x . Corrections

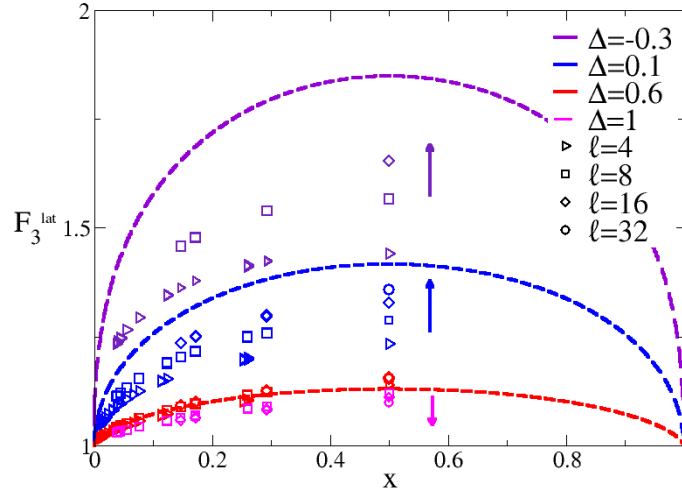


Figure 20. TTN data for $F_3^{\text{lat}}(x)$ as function of x for various sizes of the chain, $\Delta = -0.3, 0.1, 0.6, 1$, and subsystem lengths $\ell = 4, 8, 16, 32$. We denote with different symbols the values of ℓ and with different colors the various Δ . The dashed curves are the theoretical results given by Eq. (7). The arrows denote the (asymptotically) increasing subsystem sizes ℓ .

to the scaling are non-monotonic in the range $0.2 \leq \Delta \leq 0.7$. This phenomenon can be understood if further corrections to the scaling are taken into account. There are two corrections that can be responsible of this behavior. On the one hand, corrections of the form ℓ^{-mK_L} (from $\ell^{-2mK_L/n}$ at $n = 2$) for any integer m are known to be present [35], on the other hand usual analytic corrections such as ℓ^{-1} are generically expected to exist for any quantity from general scaling arguments. Thus the most general finite- ℓ ansatz has the form

$$F_2^{\text{lat}}(x) = F_2^{\text{CFT}}(x) + \frac{f_2(x)}{\ell^{K_L}} + \frac{f_A(x)}{\ell} + \frac{f_B(x)}{\ell^{2K_L}} \dots, \quad (71)$$

where the first correction is the *unusual* one employed also for the Ashkin-Teller model, and the other two are the ones just discussed. The effect of subleading corrections is enhanced by the fact that the amplitude functions $f_2(x)$ and $f_A(x)$ or $f_B(x)$ have opposite signs determining the non-monotonic behavior. Unfortunately, for values of Δ for which the effect of subleading corrections is more pronounced (i.e. $0.1 \leq \Delta \leq 0.6$), we have $K_L < 1 < 2K_L$, making difficult to disentangle corrections with close exponents. Thus, in order to present analyses of a good quality, we ignore the last correction (i.e. we fix $f_B(x) = 0$). To check the proposed scenario, we performed the fit of the data in Fig. 19 with the ansatz (71) and $f_B(x) = 0$. The results of the fits are reported in the same figure, showing perfect agreement with the data for all the values of Δ . We repeated the same analysis for other values of x , finding the same quality of fits as for $x = 1/2$. However, we cannot exclude that corrections of the form ℓ^{-2K_L} have an important role.

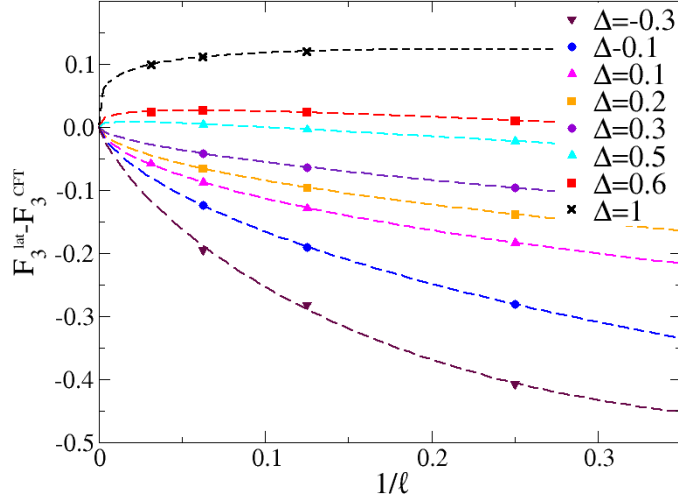


Figure 21. TTN data for $F_3^{\text{lat}}(x)$ at fixed $x = 1/2$ as function of ℓ^{-1} for $\ell = 4, 8, 16, 32$. The considered values of Δ are $\Delta = -0.3, -0.1, 0.1, 0.6, 1$. The dashed curves are fits with the ansatz (72)

6.3. Double interval: the $n = 3$ case.

Now we report the same analysis performed for $\text{Tr} \rho_A^2$ for the third moment of ρ_A , i.e. $\text{Tr} \rho_A^3$. Again we consider finite-size XXZ spin-chains and extract the universal function $F_3^{\text{CFT}}(x)$ by finite-size analysis. The expected CFT result is given for general n by Eq. (7). In Fig. 20 we show TTN data for $F_3^{\text{lat}}(x)$ (obtained from Eq. (56)) at $\Delta = -0.3, 0.1, 0.6, 1$ and subsystem sizes up to $\ell = 32$. We also show the theoretical curves given by Eq. (7). As for the $n = 2$, the asymptotic universal curve is approached from below for $\Delta \leq 0.6$, and from above for $\Delta \geq 0.6$. Furthermore, the behavior of the numerical data for $\Delta > 0.6$ is non monotonic. This suggests that the ansatz in Eq. (57) is not enough to describe accurately the TTN data and further corrections to the scaling should be included as for $\text{Tr} \rho_A^2$.

For $n = 3$, the leading corrections to the scaling are described by the ansatz (57), i.e. the leading exponent is $2K_L/3$. Thus, for the cases when subleading corrections are more important (i.e. for $\Delta \geq 0.6$) the ordering of the exponents is $2K_L/3 < 4K_L/3 < 1$ and so it is reasonable to ignore the analytic correction. Thus we fit TTN data with the function

$$F_3^{\text{lat}}(x) - F_3^{\text{CFT}}(x) = f_3(x)\ell^{-2K_L/3} + f_B(x)\ell^{-4K_L/3}. \quad (72)$$

In Fig. 21 we report TTN data for $F_3^{\text{lat}}(x) - F_3^{\text{CFT}}(x)$ for $x = 1/2$ and several values of Δ . The dashed lines are fits with the finite-size ansatz (72), that perfectly reproduce the data.

6.4. Double interval: The von Neumann entropy.

TTN gives access to the full spectrum of the reduced density matrix of $A_1 \cup A_2$ and so to the entanglement entropy $S_1^{(n)}$ as well. In Fig. 22 we report the function $F_{VN}^{\text{lat}}(x)$

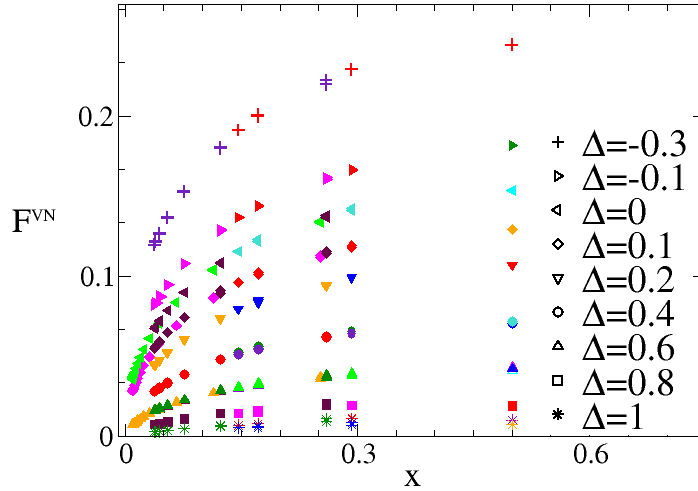


Figure 22. TTN data for the von Neumann entropy for various values of Δ in the interval $[-0.3, 1]$. We show with different symbols the values of Δ while different colors stand for different ℓ and lattice sizes.

defined as

$$F_{VN}^{\text{lat}}(x) = S_{A_1 \cup A_2}^{(1)} - S_{A_1}^{(1)} - S_{A_2}^{(1)} - \frac{1}{3} \log(1-x), \quad (73)$$

for Δ in the interval $[-0.3, 1]$ for various L up to 128 and subsystem sizes $\ell = 2, 4, 8, 16, 32, 64$. We indicate with different symbols different values of Δ , while the colors are for various sizes ℓ . As known from many other investigations on single and double intervals (quantum Ising spin chain, XY model, XXZ) the von Neumann entropy does not show oscillations with the parity of the subsystem and the corrections are much smaller, actually negligible from any practical porpouse. Fig. 22 confirms this observation for the two interval entanglement entropy for the XXZ spin-chain in a wide range of Δ . Indeed, at fixed value of Δ perfect data collapse is observed even for very small values of ℓ .

Unfortunately, as already stated in the introduction, the CFT prediction for $F_{VN}(x)$ is unknown for general x because the analytic continuation of $F_n(x)$ to non-integer n is not achievable. However, an expression for the leading term of the small x expansion of $F_{VN}(x)$ has been recently extracted [30] from Eq. (13)

$$F_{VN}(x) = \left(\frac{x}{4}\right)^\alpha \sqrt{\pi} \frac{\Gamma(\alpha+1)}{2\Gamma(\alpha+3/2)}, \quad (74)$$

where $\alpha = \min[\eta, 1/\eta]$ and Γ is the Euler function (not to be confused with the Γ matrix in Eq. (8)). In order to check the correctness of this formula, in Fig. 23 we report the same data for $F_{VN}(x)$ in a log-log scale to highlight the power-law behavior for small x . We also report the small x expected from Eq. (74). For $\Delta = -0.3$ the agreement is good, but it gets worse increasing Δ . The natural explanation is that

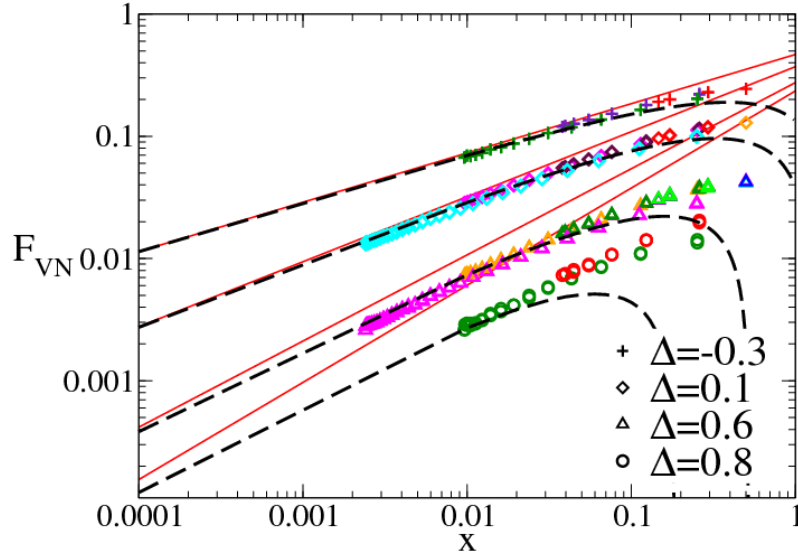


Figure 23. TTN data for the von Neumann entropy for $\Delta = -0.3, 0.1, 0.6, 0.8$ (the data for different Δ are denoted with different symbols) in log-log scale. We used different colors to indicate the different block sizes ℓ and lattice sizes L . The continuous lines are the small x behavior obtained from (74). The dashed lines are the small x behavior where the $O(x)$ term has been added as in Eq. (75).

the considered values of x are not small enough for the asymptotic Eq. (74) to be valid. We should then include further terms in the small x expansion. As explained in Ref. [30], further coefficients in the expansion for small x are difficult to obtain in general. However, there is a term that is very easy to obtain and that (luckily enough) is responsible of the previous disagreement. Indeed, as shown in Ref. [30] (cf. Eq. 70 and 71 there) the function $F_n(x)$ has always (i.e. independently of η) a simple $O(x)$ contribution coming from the denominator in Eq. (7), i.e. $|\Theta(0|\Gamma)|^2 = 1 + x(n-1)/n/6$, that can be easily analytically continued giving

$$F_{VN}(x) = \left(\frac{x}{4}\right)^\alpha \sqrt{\pi} \frac{\Gamma(\alpha+1)}{2\Gamma(\alpha+3/2)} - \frac{x}{3} + O(x^{2\alpha}). \quad (75)$$

Notice that the added term becomes more important when α is close to 1, i.e. in the XXZ spin-chain when Δ approaches 1. In Fig. 23 we also report the prediction (75) as dashed line, that is asymptotically in perfect agreement with the numerical data for all values of Δ .

7. Conclusions

In this manuscript we provided a number of results for the asymptotic scaling of the Rényi entanglement entropies in strongly interacting lattice models described by CFTs with $c = 1$. Schematically our results can be summarized as follows.

- We provided the analytic CFT result for the scaling function $F_2(x)$ for $S_A^{(2)}$ in the case of a free boson compactified on an orbifold describing, among the other things, the scaling limit of the Ashkin-Teller model on the self-dual line. The final result is given in Eq. (25).

- We developed a cluster Monte Carlo algorithm for the two-dimensional Ashkin-Teller model (generalizing the procedure of Caraglio and Gliozzi [18] for the Ising model) that gives the scaling functions of the Rényi entanglement entropy (for integer n) of the corresponding one-dimensional quantum model. With this algorithm, we calculated numerically the scaling function $F_2(x)$ of the AT model along the self-dual line and we confirm the validity of the CFT prediction. In order to obtain a quantitative agreement, the corrections to scaling induced by the finite length of the blocks are properly taken into account.
- We considered the XXZ spin chains by means of a tree tensor network (TTN) algorithm. The low-energy excitations of model are described by a free boson compactified on a circle for which CFT predictions are already available both for $n = 2$ [17] and for general integer n [19]. Taking into account the corrections to the scaling, we confirm these predictions (that resisted until now to quantitative tests) for $n = 2, 3$. Furthermore, we provide numerical determinations of the scaling function of the von Neumann entropy (cf. Fig. 22) for which CFT predictions do not exist yet for general x . For small x we confirm the recent prediction of Ref. [30] (cf. Fig. 23).

The methods we employed (classical Monte Carlo with cluster observables and TTN) are very general techniques that can be easily adapted to other models of physical interest. On the CFT side, it must be mentioned that a closed form for the functions $F_n(x)$ at integer n for a free boson compactified on an orbifold is not yet available, but work in this direction is in progress [70].

Acknowledgments

We thank John Cardy, Maurizio Fagotti, Erik Tonni, Ettore Vicari, and Guifre Vidal for useful discussions. This work has been partly done when PC was guest of the Galileo Galilei Institute in Florence whose hospitality is kindly acknowledged.

References

- [1] L Amico, R Fazio, A Osterloh, and V Vedral, Entanglement in many-body systems, *Rev. Mod. Phys.* **80**, 517 (2008); J Eisert, M Cramer, and M B Plenio, Area laws for the entanglement entropy - a review, *Rev. Mod. Phys.* **82**, 277 (2010); Entanglement entropy in extended systems, P Calabrese, J Cardy, and B Doyon Eds, *J. Phys. A* **42** 500301 (2009).
- [2] P. Calabrese and A. Lefevre, Entanglement spectrum in one-dimensional systems, *Phys. Rev. A* **78**, 032329 (2008).
- [3] N Schuch M M Wolf, F Verstraete, and J I Cirac, Entropy scaling and simulability by matrix product states, *Phys. Rev. Lett.* **100**, 030504 (2008); D Perez-Garcia, F Verstraete, M M Wolf, J I Cirac, Matrix Product State Representations *Quantum Inf. Comput.* **7**, 401 (2007); L Tagliacozzo, T R. de Oliveira, S Iblisdir, and J I Latorre, Scaling of entanglement support for Matrix Product States, *Phys. Rev. B* **78**, 024410 (2008); F Pollmann, S Mukerjee, A M Turner, and J E Moore, Theory of finite-entanglement scaling at one-dimensional quantum critical points, *Phys. Rev. Lett.* **102**, 255701 (2009).
- [4] J I Cirac and F Verstraete, Renormalization and tensor product states in spin chains and lattices, *J. Phys. A* **42** (2009) 504004.
- [5] C. Holzhey, F. Larsen, and F. Wilczek, Geometric and renormalized entropy in conformal field theory, *Nucl. Phys. B* **424**, 443 (1994).
- [6] P. Calabrese and J. Cardy, Entanglement entropy and quantum field theory, *J. Stat. Mech.* P06002 (2004).
- [7] G. Vidal, J. I. Latorre, E. Rico, and A. Kitaev, Entanglement in quantum critical phenomena, *Phys. Rev. Lett.* **90**, 227902 (2003); J. I. Latorre, E. Rico, and G. Vidal, Ground state entanglement in quantum spin chains, *Quant. Inf. Comp.* **4**, 048 (2004).

- [8] P. Calabrese and J. Cardy, Entanglement entropy and conformal field theory, *J. Phys. A* **42**, 504005 (2009).
- [9] M Fagotti, P Calabrese, and J E Moore, Entanglement spectrum of random-singlet quantum critical points, *Phys. Rev. B* **83**, 045110 (2011).
- [10] J. Cardy, The ubiquitous 'c': from the Stefan-Boltzmann law to quantum information, *J. Stat. Mech.* (2010) P10004.
- [11] Al. B. Zamolodchicov, Conformal scalar field on the hyperelliptic curve and critical Ashkin-Teller multipoint correlation functions, *Nucl. Phys. B* **285** (1987) 481.
- [12] P Ginsparg, Applied conformal field theory, in: *Les Houches, session XLIX (1988), Fields, strings and critical phenomena*, Eds. E. Brézin and J. Zinn-Justin, Elsevier, New York (1989).
- [13] R Dijkgraaf, E P Verlinde and H L Verlinde, $c = 1$ Conformal Field Theories on Riemann Surfaces, *Commun. Math. Phys.* **115** (1988) 649.
- [14] P Ginsparg, Curiosities at $c = 1$, *Nucl. Phys. B* **295** (1988) 153; G Harris, SU(2) current algebra orbifolds of the gaussian model, *Nucl. Phys. B* **300** (1988) 588.
- [15] H. W. Blöte, J. L. Cardy, and M. P. Nightingale, Conformal invariance, the central charge, and universal finite-size amplitudes at criticality, *Phys. Rev. Lett.* **56** (1986), 742; I. Affleck, Universal term in the free energy at a critical point and the conformal anomaly, *Phys. Rev. Lett.* **56** (1986), 746.
- [16] B. Hsu, M. Mulligan, E. Fradkin, and E.-A. Kim, Universal entanglement entropy in 2D conformal quantum critical points, *Phys. Rev. B* **79**, 115421 (2009); J.-M. Stephan, S. Furukawa, G. Misguich, and V. Pasquier; Shannon and entanglement entropies of one- and two-dimensional critical wave functions, *Phys. Rev. B* **80**, 184421 (2009); M Oshikawa, Boundary Conformal Field Theory and Entanglement Entropy in Two-Dimensional Quantum Lifshitz Critical Point, 1007.3739.
- [17] S. Furukawa, V. Pasquier, and J. Shiraishi, Mutual information and compactification radius in a $c=1$ critical phase in one dimension, *Phys. Rev. Lett.* **102**, 170602 (2009).
- [18] M. Caraglio and F. Gliozzi, Entanglement entropy and twist fields, *JHEP* 0811: 076 (2008).
- [19] P Calabrese, J Cardy, and E Tonni, Entanglement entropy of two disjoint intervals in conformal field theory, *J. Stat. Mech.* P11001 (2009).
- [20] H Casini and M Huerta, A finite entanglement entropy and the c -theorem, *Phys. Lett. B* **600** (2004) 142; H Casini, C D Fosco, and M Huerta, Entanglement and alpha entropies for a massive Dirac field in two dimensions, *J. Stat. Mech.* P05007 (2005); H Casini and M Huerta, Remarks on the entanglement entropy for disconnected regions, *JHEP* 0903: 048 (2009); H Casini and M Huerta, Reduced density matrix and internal dynamics for multicomponent regions, *Class. Quant. Grav.* **26**, 185005 (2009); H Casini, Entropy inequalities from reflection positivity, *J. Stat. Mech.* (2010) P08019.
- [21] P. Facchi, G. Florio, C. Invernizzi, and S. Pascazio, Entanglement of two blocks of spins in the critical Ising model, *Phys. Rev. A* **78**, 052302 (2008).
- [22] I. Klich and L. Levitov, Quantum noise as an entanglement meter, *Phys. Rev. Lett.* **102**, 100502 (2009).
- [23] S. Ryu and T. Takayanagi, Holographic derivation of entanglement entropy from AdS/CFT, *Phys. Rev. Lett.* **96** (2006) 181602; S. Ryu and T. Takayanagi, Aspects of holographic entanglement entropy, *JHEP* 0608: 045 (2006); V. E. Hubeny and M. Rangamani, Holographic entanglement entropy for disconnected regions, *JHEP* 0803: 006 (2008); M Headrick and T Takayanagi, A holographic proof of the strong subadditivity of entanglement entropy, *Phys. Rev. D* **76**, 106013 (2007); T. Nishioka, S. Ryu, and T. Takayanagi, Holographic entanglement entropy: an overview, *J. Phys. A* **42** (2009) 504008; E Tonni, Holographic entanglement entropy: near horizon geometry and disconnected regions, 1011.0166.
- [24] V. Alba, L. Tagliacozzo, and P. Calabrese, Entanglement entropy of two disjoint blocks in critical Ising models, *Phys. Rev. B* **81** (2010) 060411.
- [25] F Igloi and I Peschel, On reduced density matrices for disjoint subsystems, 2010 EPL 89 40001.
- [26] M Fagotti and P Calabrese, Entanglement entropy of two disjoint blocks in XY chains, *J. Stat. Mech.* (2010) P04016.
- [27] M Headrick, Entanglement Renyi entropies in holographic theories, *Phys. Rev. D* **82**, 126010 (2010).
- [28] M Fagotti and P Calabrese, Universal parity effects in the entanglement entropy of XX chains with open boundary conditions, *J. Stat. Mech.* P01017 (2011).
- [29] P Calabrese, Entanglement entropy in conformal field theory: New results for disconnected regions, *J. Stat. Mech.* (2010) P09013.
- [30] P Calabrese, J Cardy, and E Tonni, Entanglement entropy of two disjoint intervals in conformal field theory II, *J. Stat. Mech.* P01021 (2011).

- [31] H. Wichterich, J. Molina-Vilaplana, and S. Bose, Scale invariant entanglement at quantum phase transitions, *Phys. Rev. A* **80**, 010304(R) (2009); S. Marcovitch, A. Retzker, M. B. Plenio, and B. Reznik, Critical and noncritical long range entanglement in the Klein-Gordon field, *Phys. Rev. A* **80**, 012325 (2009); H. Wichterich, J. Vidal, and S. Bose, Universality of the negativity in the Lipkin-Meshkov-Glick model, *Phys. Rev. A* **81**, 032311 (2010).
- [32] J. Cardy, Measuring entanglement using quantum quenches, 1012.5116.
- [33] F C Alcaraz, M I Berganza, and G Sierra, Entanglement of low-energy excitations in Conformal Field Theory, 1101.2881.
- [34] P. Calabrese, M. Campostrini, F. Essler, and B. Nienhuis, Parity effects in the scaling of block entanglement in gapless spin chains, *Phys. Rev. Lett.* **104**, 095701 (2010).
- [35] P. Calabrese and F. H. L. Essler, Universal corrections to scaling for block entanglement in spin-1/2 XX chains, *J. Stat. Mech.* (2010) P08029.
- [36] J. Cardy and P. Calabrese, Unusual corrections to scaling in entanglement entropy, *J. Stat. Mech.* (2010) P04023.
- [37] P. Calabrese, J. Cardy, and I. Peschel, Corrections to scaling for block entanglement in massive spin-chains, *J. Stat. Mech.* (2010) P09003; M Campostrini and E Vicari, Scaling of bipartite entanglement in one-dimensional lattice systems, with a trapping potential, *J. Stat. Mech.* (2010) P08020; E Ercolessi, S Evangelisti, F Franchini, and F Ravanini, Essential singularity in the Renyi entanglement entropy of the one-dimensional XYZ spin-1/2 chain, *Phys. Rev. B* **83**, 012402 (2011).
- [38] J C Xavier and F C Alcaraz, Renyi Entropy and Parity Effect of the Anisotropic Spin-s Heisenberg Chains with a Magnetic Field, 1103.2103.
- [39] P. Calabrese and J. Cardy, Entanglement entropy and quantum field theory: a non-technical introduction, *Int. J. Quant. Inf.* **4**, 429 (2006).
- [40] L. J. Dixon, D. Friedan, E. J. Martinec and S. H. Shenker, The conformal field theory of orbifolds, *Nucl. Phys. B* **282** (1987) 13.
- [41] J Cardy, Operator content of two-dimensional conformally invariant theories, *Nucl. Phys. B* **270** (1986) 186; A Cappelli, C Itzykson, and J-B Zuber, Modular invariant partition functions in two dimensions, *Nucl. Phys. B* **280** (1987) 445; C Itzykson and J-B Zuber, Two-dimensional conformal invariant theories on a torus, *Nucl. Phys. B* **275** (1986) 580; P Di Francesco, H Saleur, and J-B Zuber, Modular invariance in non-minimal two-dimensional conformal theories, *Nucl. Phys. B* **285** (1987) 454; V Pasquier, Lattice derivation of modular invariant partition functions on the torus, 1987 *J. Phys. A* **20**, L1229.
- [42] H Saleur, Partition functions of the two-dimensional Ashkin-Teller model on the critical line, 1987 *J. Phys. A* **20** L1127; S. K. Yang, Modular invariant partition function of the Ashkin-Teller model on the critical line and $N = 2$ superconformal invariance, *Nucl. Phys. B* **285** (1987) 183; H Saleur, Correlation functions of the critical Ashkin-Teller model on a torus, *J. Stat. Phys.* **50** (1988) 475.
- [43] L Alvarez-Gaume, J B Bost, G W Moore, P C Nelson, and C Vafa, Bosonization on higher genus Riemann surfaces, *Commun. Math. Phys.* **112** (1987) 503; D Bernard, Z_2 -twisted fields and bosonization on Riemann surfaces, *Nucl. Phys. B* **302** (1988) 251.
- [44] V. Alba, M. Fagotti, and P. Calabrese, Entanglement entropy of excited states, *J. Stat. Mech.* (2009) P10020.
- [45] R J Baxter, *Exactly Solved Models in Statistical Mechanics*, 1982 Academic Press, San Diego.
- [46] L. P. Kadanoff and A. C. Brown, Correlation functions on the critical lines of the Baxter and Ashkin-Teller models, *Ann. Phys.* **121** (1979) 318; J Cardy, Continuously varying exponents and the value of the central charge, *J. Phys. A* **20** (1987) L891.
- [47] S Wiseman and E Domany, Cluster method for the Ashkin-Teller model, *Phys. Rev. E* **48**, 4080 (1993).
- [48] J Salas and A D Sokal, Dynamic critical behavior of a Swendsen-Wang-type algorithm for the Ashkin-Teller model, *J. Stat. Phys.* **85**, 297 (1996).
- [49] M B Hastings, I Gonzalez, A B Kallin, and R G Melko Measuring Renyi Entanglement Entropy with Quantum Monte Carlo, *Phys. Rev. Lett.* **104**, 157201 (2010); R G Melko, A B Kallin, and M B Hastings, Finite Size Scaling of Mutual Information: A Scalable Simulation, *Phys. Rev. B* **82**, 100409(R) (2010).
- [50] F. Igloi and R. Juhasz, Exact relationship between the entanglement entropies of XY and quantum Ising chains, *Europhys. Lett.* **81**, 57003 (2008).
- [51] B.-Q. Jin and V. E. Korepin, Quantum spin chain, Toeplitz determinants and Fisher-Hartwig conjecture, *J. Stat. Phys.* **116**, 79 (2004).
- [52] J. L. Cardy, O.A. Castro-Alvaredo, and B. Doyon, Form factors of branch-point twist fields in quantum integrable models and entanglement entropy, *J. Stat. Phys.* **130** (2008) 129.

- [53] L Tagliacozzo, G Evenbly, and G Vidal, Simulation of two-dimensional quantum systems using a tree tensor network that exploits the entropic area law, *Phys. Rev. B* **80**, 235127 (2009).
- [54] M. Fannes, B. Nachtergaele, and R. F. Werner, Ground states of VBS models on Cayley trees, *J. Stat. Phys.* **66**, 939 (1992).
- [55] B Friedman, A density matrix renormalization group approach to interacting quantum systems on Cayley trees, *J. Phys.: Cond. Matt.* **42**, 9021 (1997).
- [56] Y Hieida, K Okunishi, and Y Akutsu, Numerical renormalization approach to two-dimensional quantum antiferromagnets with valence-bond-solid type ground state, *New J. Phys.* **1**, 7 (1999).
- [57] M-B Lepetit, M Cousy, and G M Pastor, Density-matrix renormalization study of the Hubbard model on a Bethe lattice, *Eur. Phys. J. B*, **13**, 421 (2000).
- [58] M A Martin-Delgado, J Rodriguez-Laguna, and G Sierra, Density-matrix renormalization-group study of excitons in dendrimers, *Phys. Rev. B* **65**, 155116 (2002).
- [59] Y-Y Shi, L-M Duan, and G Vidal, Classical simulation of quantum many-body systems with a tree tensor network *Phys. Rev. A* **74**, 022320 (2006).
- [60] D Nagaj, E Farhi, J Goldstone, P Shor, and I Sylvester, Quantum transverse-field Ising model on an infinite tree from matrix product states, *Phys. Rev. B* **77**, 214431 (2008).
- [61] P Silvi, V Giovannetti, S Montangero M Rizzi, J I Cirac, and R Fazio, Homogeneous binary trees as ground states of quantum critical Hamiltonians, *Phys. Rev. A* **81**, 062335 (2010).
- [62] R Hübener, V Nebendahl, and W Dür, Concatenated tensor network states, *New J. Phys.* **12**, 025004 (2010).
- [63] V Murg, F Verstraete, O Legeza, and R M Noack, Simulating strongly correlated quantum systems with tree tensor networks, *Phys. Rev. B* **82**, 205105 (2010).
- [64] R Hübener, C Kruszynska, L Hartmann, W Dür, M B Plenio, and J Eisert, Renormalization algorithm with graph enhancement, 1101.1874.
- [65] F Gliozzi and L Tagliacozzo, Entanglement entropy and the complex plane of replicas, *J. Stat. Mech.* P01002 (2010).
- [66] L Tagliacozzo and G Vidal, Entanglement renormalization and gauge symmetry, 1007.4145.
- [67] B Nienhuis, M Campostrini, and P Calabrese, Entanglement, combinatorics and finite-size effects in spin-chains, *J. Stat. Mech.* (2009) P02063; J Sato and M Shiroishi, Density matrix elements and entanglement entropy for the spin-1/2 XXZ chain at $\Delta=1/2$, *J. Phys. A* **40**, 8739 (2007); J Damerau, F Göhmann, N P Hasencllever, and A Klümper, Density matrices for finite segments of Heisenberg chains of arbitrary length, *J. Phys. A* **40**, 4439 (2007); J Sato, M Shiroishi, and M Takahashi, Exact evaluation of density matrix elements for the Heisenberg chain, *J. Stat. Mech.* P12017 (2006); L Banchi, F Colomo, and P Verrucchi, When finite-size corrections vanish: The $S=1/2$ XXZ model and the Razumov-Stroganov state, *Phys. Rev. A* **80**, 022341 (2009); E Ercolessi, S Evangelisti, and F Ravanini, Exact entanglement entropy of the XYZ model and its sine-Gordon limit *Phys. Lett. A* **374**, 2101 (2010); O A Castro-Alvaredo and B Doyon, Permutation operators, entanglement entropy, and the XXZ spin chain in the limit *J. Stat. Mech.* (2011) P02001.
- [68] N Laflorencie, E S Sorensen, M-S Chang, and I Affleck, Boundary effects in the critical scaling of entanglement entropy in 1D systems, *Phys. Rev. Lett.* **96**, 100603 (2006).
- [69] G De Chiara, S Montangero, P Calabrese, and R Fazio, Entanglement entropy dynamics in Heisenberg chains, *J. Stat. Mech.* (2006) P03001; J C Xavier, Entanglement entropy, conformal invariance and the critical behavior of the anisotropic spin-S Heisenberg chains: A DMRG study, *Phys. Rev. B* **81**, 224404 (2010); H F Song, S Rachel, and K Le Hur, General relation between entanglement and fluctuations in one dimension, *Phys. Rev. B* **82**, 012405 (2010).
- [70] P Calabrese and E Tonni, in progress.